Fe-TiC-H machine learning interatomic potential for predicting hydrogen segregation and diffusion in TiC/Fe

Saurabh Sagar and Poulumi Dey*
Department of Materials Science and Engineering, Faculty of Mechanical Engineering, Delft University of Technology, Mekelweg 2, 2628 CD, Netherlands

Francesco Maresca
Mechanics of Materials, Engineering and Technology Institute Groningen, Faculty of Science and Engineering, University of Groningen, Nijenborgh 4, Groningen 9747 AG, Netherlands

(Received 26 September 2025; accepted 12 May 2026; published 5 June 2026)

Carbide particles act as effective hydrogen traps that can mitigate hydrogen embrittlement in steels, with their trapping efficacy governed by the binding energy of hydrogen at atomic-scale sites within the carbide and at the carbide/matrix interface. Within the carbide, carbon vacancies are established trap sites, while at the carbide/matrix interface, multiple distinct trap sites may form depending upon the interface character. State-of-the-art experimental methods cannot attribute binding energies to individual sites unambiguously, particularly at the carbide/matrix interface, where distinct trap sites may exhibit similar binding energies. Density functional theory (DFT) calculations have partially addressed this limitation, but their computational cost prohibits accurate treatment of semicoherent and incoherent interfaces, for which hydrogen binding energies remain poorly characterised. In this work, we develop a DFT-accurate machine-learning Fe–TiC–H interatomic potential that enables simulations of hydrogen energetics and kinetics at various TiC/Fe interfaces in the Baker–Nutting orientation. Predictions of structural, dynamic and energetic properties of both bulk phases (i.e., bcc Fe and rocksalt TiC) and the coherent interface with and without hydrogen are in good agreement with DFT. We apply the potential to examine the atomic structure and hydrogen trapping at semicoherent and incoherent interfaces. We find that the binding energy of hydrogen at misfit dislocations is similar to that at coherent interfaces, with a difference of no more than 0.1 eV. However, the misfit strain field reduces carbon vacancy formation energies at the interface, where hydrogen can be trapped with similar binding energies as that in a bulk C vacancy (approximately –1 eV). Lower vacancy formation energies are also found at the incoherent interface, where hydrogen binding energies span a broader range, depending sensitively on the local atomic environment. Overall, the results enable interpretation of experimental observations of hydrogen segregation around semicoherent and incoherent TiC interfaces.

DOI: 10.1103/75wj-b4n1

I. INTRODUCTION

Hydrogen embrittlement (HE) poses a major challenge to the steel-making industry, as improvements in mechanical strength are generally accompanied by increased HE susceptibility [1–4]. Ferritic steels micro-alloyed with carbide/carbonitride-forming elements (Ti, V, Nb, Mo) are an exception to this general trend [5–12]. The reduced HE susceptibility of these materials is attributed to the hydrogen trapping characteristics of the carbides [13–22]. Atomic hydrogen, because of its high mobility, diffuses freely through the pristine ferrite matrix. Microstructural defects, however, can act as hydrogen traps, leading to the concentration of hydrogen in these regions. The occurrence of a critical local hydrogen concentration around vulnerable defects such as cracks and voids is considered to be a necessary precursor for the onset of HE [23–26]. Carbide particles can compete with these defects by trapping substantial amounts of hydrogen through the strong binding of hydrogen to carbide/matrix interfaces and carbon vacancies [27–31]. This leads to a reduced hydrogen chemical potential and effective diffusivity in the material, preventing the fast diffusion and accumulation of hydrogen around harmful defects.

The trapping efficacy of a carbide particle is governed by the binding energy of hydrogen at various atomic-scale trapping sites within the carbide. Among these, carbon vacancies are known to have the strongest binding, especially in carbides of Group IV elements, i.e., Ti, Zr, and Hf, mediated by a prominent charge redistribution around the hydrogen atom [27,30,32,33]. Beyond vacancies, the carbide/matrix interface presents additional trapping sites whose nature and strength vary with the interface character [27,34]. Rock salt carbides

*Contact author: p.dey@tudelft.nl

Published by the American Physical Society under the terms of the Creative Commons Attribution 4.0 International license. Further distribution of this work must maintain attribution to the author(s) and the published article's title, journal citation, and DOI.

precipitated in the ferrite matrix adopt the Baker–Nutting orientation with the ferrite [35]. Their morphology and interface character are governed by the growth conditions during heat treatment [36]. The smallest carbides (a few nanometers) are in the shape of thin platelets or disks, where the broad face is fully coherent with the ferrite matrix. Because of the lattice mismatch between the two phases, elastic strains are formed at the interface. Beyond a critical size, misfit dislocations form to partially relieve the coherency strains, partitioning the interface into coherent regions periodically separated by dislocation cores. Such an interface morphology is therefore referred to as semicoherent [36,37]. Further growth of the carbides leads to loss of coherency at the broad face, rendering the interface incoherent [38,39]. For each interface type, the side interface (i.e., along the thickness of the platelets) can either contain misfit dislocations or be completely incoherent. The coherency strain field and the misfit-dislocation cores, along with their surrounding strain fields, are possible hydrogen trap sites at the coherent and semicoherent interface, while the trapping sites at the incoherent interface are less well defined owing to their distorted structure.

The binding energies of hydrogen in different carbides are estimated experimentally with thermal desorption spectroscopy (TDS) or hydrogen permeation tests [14,16–19,22,34,38,40–46]. Among the various carbides, TiC exhibits the highest hydrogen binding energies, ranging from 0.2 eV to 1.5 eV, depending upon the size and coherency of the carbide [45]. The highest energies (0.6 eV to 1.5 eV) are attributed to carbon vacancies in the carbide, while weaker trapping (with energies between 0.2 and 0.6 eV) is understood to occur at the interface [17,41,47]. Attempts have been made to attribute an energy to a particular atomic-scale trap site at the interface, such as a misfit dislocation or the incoherent side interface [34]; however, it has not proven straightforward, as these methods lack the ability to resolve, with sufficient certainty, distinct traps that have similar segregation energies [48–50]. Such a task is ideally suited to first-principles methods, and several density functional theory (DFT) studies examining hydrogen trapping at sites inside the carbide and at the interface (coherency strains, interface vacancies, misfit-dislocation cores, etc.) have been conducted [27–33,51–53].

The segregation energies of hydrogen obtained with DFT [54] at coherently strained regions of the TiC/Fe interface are found to be approximately –0.2 to –0.3 eV (depending upon the local atomic environment), which fall within the range of experimental data [27,29–31]. At the core of the misfit dislocation, two separate studies obtain significantly different segregation energies of –0.49 eV and –0.27 eV [27,31]. A possible reason for this discrepancy is the finite-size effects in DFT calculations—unlike coherent interfaces that have a uniform interface, semicoherent interfaces contain coherent and misfit regions, and therefore require many more atoms in order to capture the contrasting elastic strain fields accurately, such that the computational cost becomes prohibitively large. This problem is circumvented by splitting the interface into small regions with distinct atomic environments, and using separate models for each, with supercells comprising $\sim$100 atoms [27,31]. However, the use of such supercells can lead to inaccurate atomic relaxations because of strong image interactions across periodic boundaries and the neglect of continuity between coherent and misfit regions. Studying the structure of the incoherent side interface with DFT is even more complicated owing to the lack of a well-defined orientation relationship between the carbide and the Fe matrix [34].

The broad range of experimental binding energies attributed to C vacancies also remains unresolved by DFT calculations. A value of approximately –1 eV is found in DFT studies, for vacancies located in the bulk of TiC as well as at the coherent interface [27,29–33], whereas experimental binding energies vary over a much broader range (0.6 eV–1.5 eV). It is possible that the vacancies at semicoherent or incoherent interfaces are responsible for this difference, but reliable DFT calculations for such systems have not been possible because of the finite-size limitations mentioned above.

Classical molecular dynamics (MD) is suitable for studying larger systems, yet an accurate interatomic potential that can be used to investigate the TiC/Fe system in the presence of hydrogen is currently lacking. In this work, we develop a DFT-accurate machine learning Fe–TiC–H interatomic potential that can reliably model the atomic structure and hydrogen segregation at coherent, semicoherent and incoherent side interfaces of TiC/Fe in the Baker–Nutting orientation. The potential is benchmarked against DFT and experiments for a vast range of fundamental properties of bcc Fe, rocksalt TiC, and the TiC/Fe interface, as well as the energetic and kinetic properties of hydrogen in these systems. By applying the potential to large supercells for the semicoherent interface, comprising over 10 000 atoms, we find significant differences in the atomic relaxations around the misfit dislocations in comparison with DFT, which in turn lead to more accurate predictions for the corresponding hydrogen segregation energies. We also examine the formation of C vacancies at the various interfaces, and hydrogen trapping and migration into the vacancies in detail. These results enable the assessment of the efficacy of TiC in trapping hydrogen and assisting in HE prevention.

The paper is organized as follows: In Sec. II, we outline the details of the training dataset and the machine learning protocol employed. Next, in Sec. III, we first discuss the results of performance tests of the potential against several benchmark properties, followed by the application of the potential to examine the atomic structure and hydrogen segregation at coherent, semicoherent, and incoherent TiC/Fe interfaces. Finally, in Sec. IV we discuss the implications of our findings, particularly in comparison with experimental observations, and summarize the key conclusions.

II. METHODS

Rapid developments in the field of machine learning interatomic potentials (ML-IAPs) have made it possible to extend the accuracy of DFT to the submicron scale. By fitting a flexible, high-dimensional function to a database of DFT-computed energies, forces, and stresses, ML-IAPs are capable of capturing the complexity of multi-element potential-energy surfaces without relying on a prescribed functional form [55–57]. Several formulations of ML-IAPs have been developed in the last decade with considerable success. The key distinctions among these approaches lie either in the

choice of descriptors for the local atomic environment or in the regression methodology employed. The performance and reliability of several widely adopted ML-IAPs, including the Gaussian approximation potential (GAP), neural network interatomic potential (NNIP), and atomic cluster expansion (ACE), have been systematically assessed in previous studies [58–60]. Among the available frameworks, moment tensor potentials (MTPs) have demonstrated strong performance for the fast and accurate description of multicomponent systems [61–63], prompting the selection of MTPs in the current study.

A. Moment tensor potentials

In the MTP framework, the descriptors of the atomic neighborhood are in the form of invariant polynomials, as shown briefly below. The potential energy of the system is defined as the sum of the energies of the atomic environments of N individual atoms,

$$E^{MTP} = \sum_{i=1}^{N} V(n_i), \tag{1}$$

where n_i denotes the local atomic neighborhood around atom i, defined by the relative positions of atoms and their respective atomic numbers. The function V is the potential energy of the atomic neighborhood, and can be expanded over a set of basis functions B_α as

$$V_i^{MTP} = \sum_{\alpha} \xi_\alpha B_\alpha(n_i), \tag{2}$$

where ξ_α are the coefficients that are fitted from training data. By design, the basis functions must be invariant with respect to translations, rotations, and permutations of chemically equivalent atoms. This is achieved by representing the atomic neighborhood via *moment tensors*, which have the form

$$M_{\mu,\nu}(r) = \sum_{j} f_\mu(|r_{ij}|, z_i, z_j) r_{ij}^{\otimes \nu}, \tag{3}$$

where j runs over all atoms within a predetermined cutoff radius R_c, f_μ are radial functions that depend upon the relative position vector r_{ij} and the corresponding species z_i and z_j of the atoms, while $r_{ij}^{\otimes \nu}$ encodes the angular dependence of the descriptor. The moment tensors $M_{\mu,\nu}$ are, therefore, tensors of different ranks, which are invariant to translations and permutations. The basis functions B_α are all possible contractions of $M_{\mu,\nu}$ to a scalar, making them rotationally invariant. The degree of parametrization is encoded in the *level* of the MTP, which is defined as

$$lev = 2 + 4\mu + \nu. \tag{4}$$

Thus, larger levels correspond to a higher number of fitting parameters ξ_α (with μ and ν accounting for radial and angular functions, respectively).

Detailed formulations of the radial and angular components of B_α can be found in the seminal MTP papers [61,64,65]. MTP, as coded into the MLIP-2 package, is used in this work [65]. We train MTP levels 18, 20, and 22, and optimize the cutoff radius with a grid-search algorithm.

B. Polynomial fitting

The optimization problem involves minimizing the squared difference between MTP predictions of energies (E), forces (f), and stresses (σ), and their DFT counterparts. The loss function minimization can be represented as

$$\sum_{k=1}^{K} \left[\frac{w_e}{N_k} \left(E_k^{DFT} - E_k^{MTP}\right)^2 + w_f \sum_{i=1}^{N} \left| f_{i,k}^{DFT} - f_{i,k}^{MTP} \right|^2 + \frac{w_s}{N_k} \left| \sigma_k^{DFT} - \sigma_k^{MTP} \right|^2 \right] \rightarrow \min, \tag{5}$$

where K is the total number of configurations (supercells) in the dataset and N is the total number of atoms. E_k is therefore the energy of the kth supercell, $f_{i,k}$ is the force on atom i in the kth supercell, and σ_k is the stress tensor acting on the kth supercell. We optimize the force weight w_f through a grid-search procedure, while keeping the energy and stress weights (w_e and w_s) at their default values of 1 and 0.001, respectively.

C. Training dataset

The training dataset consists of three distinct phases—bcc Fe, rocksalt TiC, and the TiC/Fe interface—each with and without hydrogen. For TiC and the TiC/Fe interface, DFT data from our previous comprehensive study on hydrogen trapping in TiC, VC, and NbC and their coherent interfaces with Fe [30] is reused. For bcc Fe, new DFT data is generated, as existing datasets [66,67] were computed with calculation parameters inconsistent with those used here. In particular, the plane-wave cutoff energy of 360 eV employed in the Fe–H dataset of Meng *et al.* [67] is insufficient for accurately modeling the dynamic properties of TiC (the cutoff energy used for TiC is 500 eV).

The complete list of configurations is shown in Table I. For each phase, pristine structures, and those with inherent point defects, i.e., vacancies and self-interstitials, and hydrogen-rich configurations are included. Random perturbations are applied to the ground state configurations, which allows for sampling of high-energy configurations. Atom positions and lattice vectors are randomly displaced following a normal distribution with standard deviations of 0.05 Å and 2.5%, respectively.[1] Additionally, in order to capture the elastic properties of Fe and TiC, configurations including stretched and sheared unit cells are also included, with the strain magnitude ranging from 0 to 2.5%.

For bulk Fe and TiC, $3 \times 3 \times 3$ and $2 \times 2 \times 2$ supercells (corresponding to 54 and 64 atoms) are used, respectively. Point-defect configurations in Fe are comprised of structures with a self-interstitial atom (SIA), vacancies and divacancies, and simple ordered vacancy structures, where all atoms lying in low index [(100), (110), and (111)] planes are removed. For TiC, since Ti vacancies have an extremely high formation energy [68,69], divacancies and ordered-vacancy structures of only C are considered. Hydrogen-rich configurations include structures with hydrogen in all unique interstices. Specifically, these are the tetrahedral and octahedral sites in Fe, and

[1]Perturbations are applied to each atom and supercell vector independently.

TABLE I. Configurations in the training dataset.

Phase	Supercell size	Remarks
Fe	$1 \times 1 \times 1$	$\pm 2.5\%$ uniaxial strain
Fe	$1 \times 1 \times 1$	0–2.5% shear strain
Fe	$3 \times 3 \times 3$	ground state
Fe	$3 \times 3 \times 3$	single Fe vacancy
Fe	$3 \times 3 \times 3$	various di-vacancy configurations
Fe	$3 \times 3 \times 3$	ordered Fe vacancies in (100), (110), and (111) planes
Fe	$3 \times 3 \times 3$	various SIA configurations
Fe–H	$1 \times 1 \times 1$	interstitial H
Fe–H	$2 \times 2 \times 2$	interstitial H
Fe–H	$3 \times 3 \times 3$	interstitial H
Fe–H	$3 \times 3 \times 3$	1–6 H in vacancy
Fe–H	$3 \times 3 \times 3$	2 interstitial H atoms at different neighbor distances
Fe–H	$3 \times 3 \times 3$	ordered configurations with 36 H atoms
TiC	$1 \times 1 \times 1$	$\pm 2.5\%$ uniaxial strain
TiC	$1 \times 1 \times 1$	0–2.5% shear strain
TiC	$2 \times 2 \times 2$	ground state and defect configurations same as Fe
TiC–H	$2 \times 2 \times 2$	same as Fe except 1–9 H in C vacancy
TiC/Fe	2×2 lateral	Fe–C, Fe–Ti and intermediate stacking (ground state for Fe–C only)
TiC/Fe	8 Fe + 6 TiC normal	vacancies and di-vacancies; SIAs without mixing (no C in Fe matrix, etc.)
TiC/Fe–H	same as above	known trap sites; 1 H atom placed on a fine grid
H	10^3 Å^3	H_2 molecule with varying bond lengths; 8 H atoms randomly distributed

tetrahedral, trigonal and face-centered sites in TiC. Configurations comprising two hydrogen atoms distributed at various nearest-neighbor distances in Fe and TiC are also included. Further, configurations of ordered distributions of hydrogen atoms, where they occupy all available interstitial sites in low-index planes, are also included. Additionally, for Fe, a single hydrogen atom in interstitial sites of a unit cell and a $2 \times 2 \times 2$ supercell is included to sample configurations representing short-range concentration regimes not captured by the $3 \times 3 \times 3$ supercell alone.

Hydrogen-vacancy interactions are captured by including various configurations with 1–6 hydrogen atoms at an Fe vacancy (all octahedral sites around the vacancy), and 1–9 hydrogen atoms at a C vacancy in TiC (all trigonal sites around the vacancy + vacancy center are filled).

The coherent interface between bcc Fe and TiC follows the Baker–Nutting orientation relationship (OR),

$$(001)_{\mathrm{Fe}} \,||\, (001)_{\mathrm{TiC}} \,,\; [100]_{\mathrm{Fe}} \,||\, [110]_{\mathrm{TiC}}$$

as is depicted in Fig. 1. Within the constraint of this OR, the two phases can be translated relative to each other along any direction in the interface plane, giving rise to different atomic stacking sequences in the interface-normal direction. The energetically favorable stacking, where C atoms sit directly above Fe atoms (Fe–C stacking), corresponds to the ground-state coherent interface structure [27,70,71], which has been used as the reference configuration throughout. [The supercell is shown in Fig. 1(b) and consists of 2×2 units of Fe in the lateral directions and eight Fe layers and six TiC layers in the interface normal direction.] Translating the carbide cell by 1/2 unit length along $[1\bar{1}0]$ and [110] yields the Fe–Ti stacking in which Ti atoms are directly on top of Fe atoms. This resembles the local atomic environment around intersecting misfit dislocations at a semicoherent interface [27,31]. An intermediate stacking, where Fe atoms lie between Ti and C atoms, approximates the environment of individual misfit dislocations [27,31]. Neither the Fe–Ti nor the intermediate stacking converges to a distinct ground state under DFT relaxation—both collapse into the Fe–C configuration. For both stacking sequences, we include single-point DFT calculations where the atom positions and supercell vectors are perturbed as described previously, which allows for sufficient sampling of these local atomic environments.

Point-defect configurations of only the coherent (Fe–C stacking) structure are included, whereas hydrogen-rich structures comprised of configurations with hydrogen in interstitial sites of the Fe and TiC sublattices are included for each

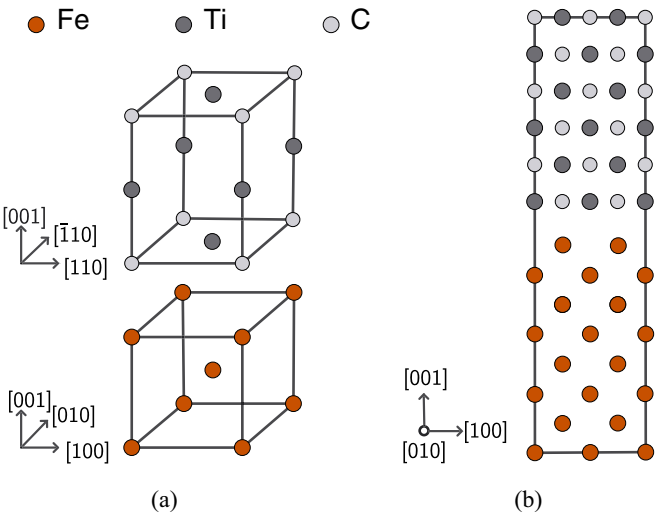


FIG. 1. The coherent TiC/Fe interface structure. (a) The Baker–Nutting OR and (b) interface supercell used in this study. Fe, C, and Ti atoms are represented by brown, light gray, and dark gray circles.

of the three stacking structures. At the interface between Fe and TiC, several stable interstitial sites are known from previous DFT studies [27,29,30], which are also taken into account. Configurations with hydrogen in Fe, C, and Ti vacancies are also included. Additionally, to sample the entire supercell uniformly, interstitial sites are identified by placing a regular grid with node spacing of 0.5 Å over the symmetry-reduced supercell.

For defect-containing and H-segregated Fe, TiC, and coherent TiC/Fe interface structures, 10% of the total dataset consists of configurations that are sampled from *ab initio* molecular dynamics (AIMD) simulations. To enable fast diffusion of atoms, AIMD simulations are performed at 900 K in the NVT ensemble by employing the deterministic Nosé–Hoover thermostat [72,73], with a time step of 0.5 fs and a total runtime of 0.5 ps. For each run, one in every 15 snapshots is sampled for the training dataset. Overall, this approach allows the generation of diverse yet thermodynamically relevant training data.

Furthermore, configurations with only H atoms are also included in the dataset. A cubic simulation cell with a side length of 10 Å is used. Two types of configurations are considered: an H_2 molecule with varying bond lengths, and eight H atoms randomly distributed in the simulation cell. The complete dataset consists of 7456 configurations and 478 137 atoms. For training the MTP, the dataset is split into a training set and a testing set, with 20% of configurations selected at random to form the testing set.

D. Computational details

All DFT calculations are performed using the Vienna *Ab initio* Simulation Package (VASP) [74]. Generalized-gradient approximation (GGA) in the formulation of Perdew, Burke, and Ernzerhof (PBE) is used for the exchange-correlation function [75], while the projector augmented-wave (PAW) method is used for the core-valence interactions [76]. A cutoff energy of 500 eV is implemented in all calculations. First-order Methfessel–Paxton smearing [77], with a width of 0.15 eV, is chosen such that the corresponding error in $T = 0$ K extrapolated energy is below 1 meV/atom. The Brillouin zone is sampled using Monkhorst–Pack grids [78]. For the interface supercells, a $10 \times 10 \times 2$ k-mesh is employed, while the $3 \times 3 \times 3$ Fe and $2 \times 2 \times 2$ TiC supercells are sampled with $8 \times 8 \times 8$ and $6 \times 6 \times 6$ k-mesh, respectively. For smaller supercells, the k-point mesh is scaled proportionally to maintain a consistent k-point density. For obtaining the ground-state configurations, a force tolerance of 0.01 eV/Å is used. The energy tolerance for the electronic self-consistency loop is set to 10^{-6} eV. Spin-polarized calculations are performed for bcc Fe and coherent TiC/Fe configurations (TiC is nonmagnetic).

MS/MD simulations are performed with the LAMMPS software package [79]. Migration barriers are estimated using the built-in implementation of the nudged elastic band (NEB) method [80,81]. Thirteen intermediate images are used in all calculations. For calculating the diffusivity of H in Fe, a $20 \times 20 \times 20$ supercell is used, which contains a total of 16 000 atoms. 1 at.% hydrogen (160 H atoms) is added to the system. Finite-temperature simulations are run at $T = 300$ K, 450 K, 600 K, 750 K, and 900 K, and five simulations are run at each temperature. The system is first equilibrated for 10 ps at the desired temperature in the NPT ensemble to obtain the relaxed lattice constants, following which, diffusion simulations are carried out in the NVT ensemble implemented with the Nosé-Hoover thermostat. The MD timestep is 0.5 fs, and the position of H atoms is tracked every 0.2 ps over a total run time of 2 ns. For TiC, a $15 \times 15 \times 15$ supercell is used, which contains 27 000 atoms. The simulation setup is identical to Fe.

To benchmark the MTP against DFT, several properties are computed. The solution enthalpy of atomic hydrogen (referred to as H hereafter) at interstitial sites in Fe and TiC is calculated using the expression

$$E_i^H = E\,[\,H_i\,] - E_0 - \mu_H, \tag{6}$$

where $E[H_i]$ is the energy of the Fe or TiC supercell containing one H in an interstitial site i, E_0 is the energy of the same supercell without H, and μ_H is the chemical potential of H, calculated as half of the energy of an isolated H_2 molecule. H segregation energy in an interstitial site at the TiC/Fe interface is defined as

$$E_{seg}^i = E\,[\,H_i\,] - E_0 - [E\,[\,FeH_T\,] - E\,[\,Fe\,]], \tag{7}$$

where $E[\,H_i\,]$ is the energy of the TiC/Fe supercell with H segregated at site i and E_0 is the energy of the same supercell without H. $E[\,FeH_T\,]$ and $E[\,Fe\,]$ are the energies of a $3 \times 3 \times 3$ bcc Fe supercell, with and without an H atom at a tetrahedral interstice, respectively. According to this definition, a negative E_{seg}^i corresponds to an energetically favorable trap site. The formation energy of a vacancy or an interstitial is defined as

$$E_F^X = E_X - E_0 - s_X \mu_X^0, \tag{8}$$

where E_X is the energy of the supercell with one vacancy or interstitial of species X, E_0 is the energy of the perfect supercell, and $s_X = +1$ for SIAs and –1 for vacancies. The energy μ_X^0 of the reference state is taken as the per-atom energy of X in its ground state. For Fe, this corresponds to its bcc structure, whereas for Ti, this is the hcp structure. For C, graphite is considered the ground state. The segregation energy of H in a vacancy is given by

$$\begin{aligned} E_{seg}^v = {} & E\,[\,nH_v\,] - E\,[\,(n-1)H_v\,] \\ & - [\,E\,[\,FeH_T\,] - E\,[\,Fe\,]], \end{aligned} \tag{9}$$

where $E[\,nH_v\,]$ is the energy of the supercell with n H atoms segregated in the vacancy.

In the aforementioned equations, the calculation of C and Ti vacancy formation energies [Eq. (8)] with MTP relies on the DFT-obtained value of μ_X^0, since the MTP is not trained on either graphite or Ti. Our DFT calculations yield values of –9.21 eV and –7.81 eV for C and Ti, respectively. All other energy terms can be calculated entirely with MTP.

III. RESULTS

In this section, the accuracy of ML is first established by presenting the errors in energies and atomic forces across the training and testing datasets. Next, the MTP is benchmarked for several elastic and energetic properties of bcc Fe, rocksalt

TABLE II. Elastic constants and bulk modulus of bcc Fe. Values are in GPa. Reference [66] is the Fe GAP, while [67] is the Fe–H NNIP.

Property	MTP	DFT (this work)	Expt. (0 K)	Other DFT	Other ML IAPs
C_{11}	239	275	240 [89]	288 [90], 258 [70]	286 [66], 296 [67]
C_{12}	133	144	136 [89]	148 [90], 133 [70]	154 [66], 147 [67]
C_{44}	125	94	121 [89]	102 [90], 94 [70]	104 [66], 96 [67]
Bulk modulus	169	188	170 [89]	195 [90], 175 [70]	198 [66]

TiC, and the coherent TiC/Fe interface, as well as the energetic and kinetic properties of H in these phases. For calculations of elastic properties of Fe and TiC, a conventional unit cell is used, whereas defect formation and H segregation in Fe and TiC are evaluated using $3 \times 3 \times 3$ and $2 \times 2 \times 2$ supercells (with 54 and 64 atoms), respectively. Properties of the coherent interface are calculated using the supercell shown in Fig. 1(b). Following benchmarking, we apply the MTP to study the atomic structure of the TiC/Fe interface (coherent, semicoherent, and incoherent), and obtain the corresponding H segregation energies and migration barriers.

A. MTP training

The accuracy of the MTP training process can be assessed by comparing the MTP predictions of energies and atomic forces in the training and testing datasets with their DFT values. Parity plots in Fig. 2 show that MTP can reproduce DFT results with high accuracy. The root mean square errors (RMSEs) in per-atom energies and atomic forces over the training dataset are 3.3 meV/atom and 75 meV/Å, respectively. The corresponding RMSEs over the testing dataset are 3.5 meV/atom and 73 meV/Å, respectively. The close agreement between training and testing RMSEs indicates reliable accuracy of the MTP without significant overfitting.

The optimized potential is a level 20 MTP. Increasing the level further to 22 leads to only a mild decrease in RMSEs, but the computational speed is reduced significantly. The optimal force weight [w_f in Eq. (5)] and cutoff radius are found to be 0.01 and 5.5 Å, respectively. Detailed hyperparameter optimization is presented in Appendix A.

B. Benchmark properties of bcc Fe and rocksalt TiC

1. Cohesive and elastic properties

The equilibrium lattice parameter of bcc Fe calculated with MTP is 2.834 Å, identical to previous DFT values (2.834 Å) [82] and close to the experimental $T = 0$ K lattice parameter (2.855 Å [83]). For TiC, the MTP lattice parameter is 4.337 Å, also in good agreement with DFT (4.33 Å [68]) and experimental (4.33 Å [84,85]) values. The energy-volume curve of both phases is shown in Fig. 3. The MTP predicts correct equilibrium volumes, and across the studied volume range, MTP-evaluated energies differ from DFT by a maximum of 2 meV/atom for Fe and 4 meV/atom for TiC. Moreover, the MTP accuracy improves at higher volumes of Fe, which is particularly relevant, as the Fe sublattice of the coherent and semicoherent TiC/Fe interface is tensile strained [29,70].

The respective bulk moduli are also shown in the insets and are listed along with the elastic constants in Tables II and III. For Fe, remarkably, the elastic constants are found to be closer to experimental values, whereas DFT and other ML IAPs (Fe GAP [66] and FeH NNIP [67]) overpredict C_{11} and the bulk modulus. One of the main reasons for the discrepancy between DFT and experiments is the well-known overbinding of Fe using the GGA functional, which leads to stronger bonding and a smaller lattice constant, and consequently, a larger bulk modulus [86–88]. For TiC, good agreement is found between MTP and both DFT and experiments, as can be seen in Table III.

2. Phonons

To assess the dynamic stability of the MTP, phonon dispersion curves of Fe and TiC along high-symmetry paths obtained at the equilibrium volume are calculated. The dynamical matrices are obtained using the finite-displacement supercell method as implemented in phonopy [93]. A $5 \times 5 \times 5$ supercell is used for Fe and a $4 \times 4 \times 4$ supercell for TiC, which are verified to yield converged phonon frequencies. The resulting dispersion spectra are shown in Fig. 4. For both Fe and TiC, the MTP can reproduce the DFT phonon dispersion with high accuracy.

3. Vacancy formation energies

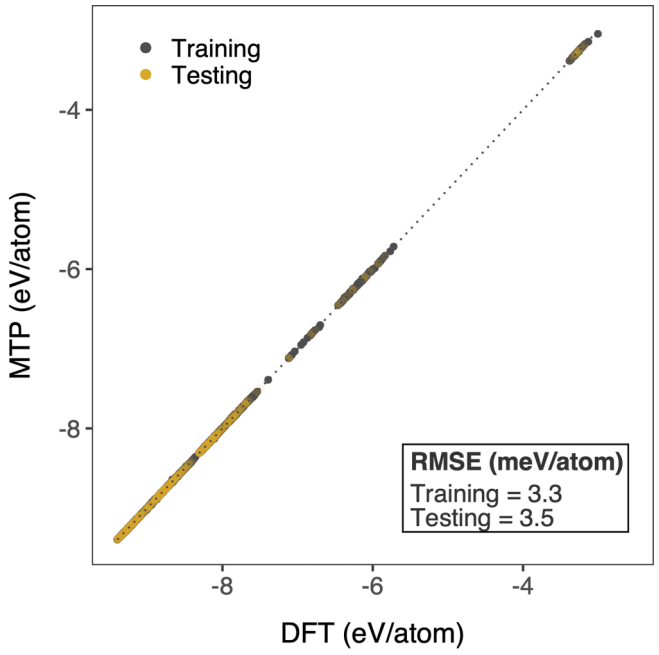
The formation energies of mono- and divacancies in Fe are shown in Fig. 5(a). The MTP predicts a monovacancy formation energy of 2.03 eV, in good agreement with our DFT value of 2.17 eV, as well as previous DFT (2.05 eV [94]; 2.15 eV [95]) and experimental (2.00 eV [96]) reports. The relative stabilities of the various divacancy configurations are also predicted accurately, with adjacent vacancies along ⟨100⟩ being the most stable, followed by ⟨111⟩. Among all configurations, a maximum difference of 0.14 eV (per vacancy) is found between the MTP and our DFT results.

Vacancy formation energies in TiC are shown in Fig. 5(b). The MTP prediction of 0.57 eV for a C vacancy is in close agreement with our DFT value of 0.62 eV, and lies within the range of reported energies obtained with different exchange-correlation functionals (0.50 eV–0.72 eV) [97]. Further, the

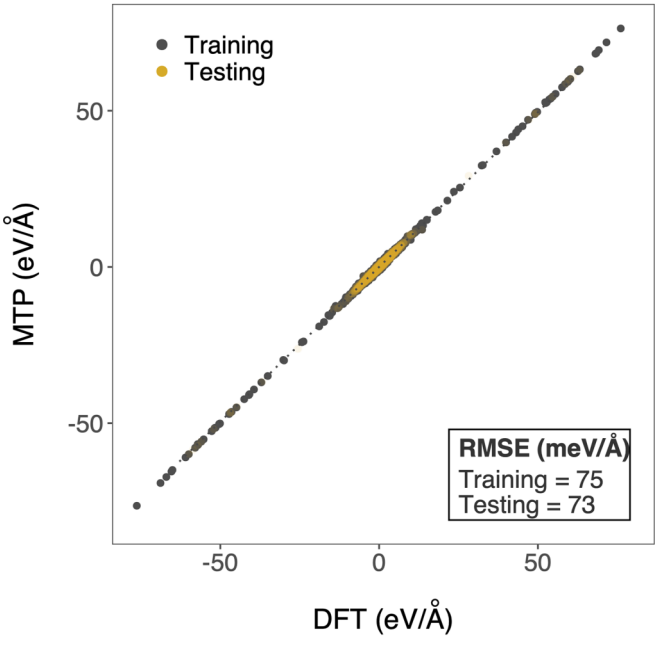
TABLE III. Elastic constants and bulk modulus of rocksalt TiC. Values are in GPa. In reference [91], two different DFT exchange-correlation functionals are employed.

Property	MTP	DFT (this work)	Expt. (298 K)	Other DFT
C_{11}	520	517	515 [92]	504 [91], 522 [91]
C_{12}	121	114	106 [92]	124 [91], 135 [91]
C_{44}	170	174	179 [92]	166 [91], 159 [91]
Bulk Modulus	254	251	242 [92]	250 [91], 264 [91]

relative stabilities of the divacancies are also predicted accurately. Adjacent vacancies along ⟨111⟩ are found to be the most stable, followed by ⟨110⟩. The same order of stabilities was also found in another DFT study; however, only relative energies of the various configurations were reported, preventing a direct comparison with our results [68]. The maximum error in MTP predictions for C vacancy formation energy in TiC is 0.05 eV. The formation energy of a Ti vacancy as obtained with MTP (8.08 eV) is also found to be similar

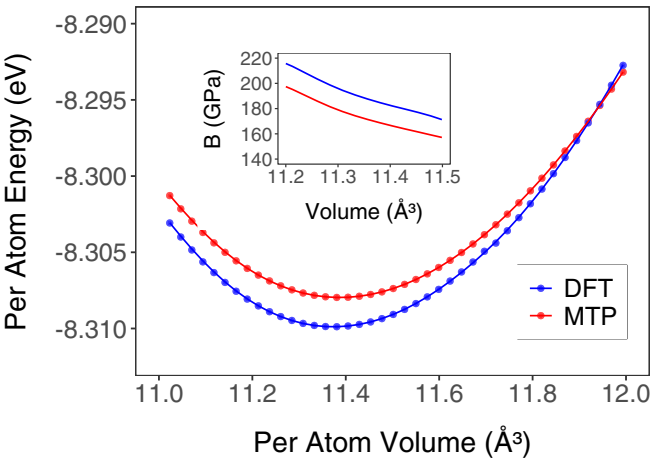


(a)

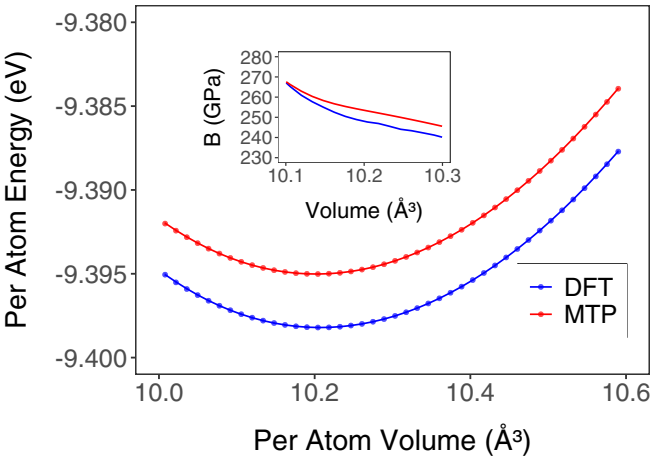


(b)

FIG. 2. Parity plots of (a) per-atom energies and (b) atomic forces between MTP and DFT for all configurations in the training and testing datasets.



(a)



(b)

FIG. 3. Equation of state predicted by MTP. (a) bcc Fe and (b) TiC. The bulk moduli calculated near the equilibrium volume are also shown in insets.

to that obtained with DFT (8.67 eV); however, because of their extremely high formation energies, Ti vacancies are not considered relevant to this work.

While vacancies are the dominant point defects in these materials, self-interstitial atoms (SIAs) can also be abundant under conditions of irradiation. Our (unpublished) DFT calculations show that SIAs in Fe and TiC are insignificant H traps. Nevertheless, the performance of the MTP for interstitial formation energies has been presented in Appendix B.

4. H trapping

H solution enthalpies in interstitial sites of Fe and TiC are listed in Table IV. In Fe, the energetic preference for tetrahedral sites is correctly predicted with MTP. The obtained solution enthalpies of 0.17 eV in the tetrahedral site and 0.25 eV in the octahedral site lie within the range of literature data obtained for various supercell sizes (0.08–0.24 eV in tetrahedral and 0.26–0.39 eV in octahedral sites). The large spread in literature data stems from the use of different Fe supercell sizes, where lower supercells yield lower solution enthalpies (see Table IV). The choice of the supercell is often motivated by the system state—for small supercells, the

TABLE IV. H solution enthalpy in bcc Fe and TiC. t- and o- refer to tetrahedral and octahedral sites in Fe, while tri- and tet- refer to trigonal and tetrahedral sites in TiC, respectively. Literature data corresponds to previous DFT and NNIP (marked with an *) reports. Supercell sizes that differ from our calculations are specified explicitly. All values are in eV.

Position	MTP	DFT (this work)	Literature (corresponding supercell size)
Fe t-site	0.17	0.21	0.08 (1 × 1 × 1) [99], 0.16 (2 × 2 × 2) [27,82], 0.19 [82], 0.20 (4 × 4 × 4) [82], 0.23 (4 × 4 × 4) [100], 0.24* [67]
Fe o-site	0.25	0.33	0.26 [101], 0.29 (2 × 2 × 2) [82], 0.32 [82], 0.37 (4 × 4 × 4) [100], 0.39* [67]
TiC, tri-site	0.71	0.71	0.84 [27]
TiC, tet-site	0.97	1.19	0.97 [32]

interaction of the H atom (and the induced strain) with its periodic images is more pronounced, and can be a useful representation of the local relaxations caused by a high H concentration, while in larger supercells, H can be isolated to a greater extent, yielding more accurate solution enthalpies.

In TiC, the preference for trigonal sites is predicted correctly, and the MTP and DFT values match exactly (0.71 eV). The solution enthalpy in a tetrahedral site is underestimated by 0.22 eV; however, there is good agreement with a previous DFT report in which the local density approximation (LDA) functional was employed [32].

The incremental segregation energies of one to six hydrogen atoms in a Fe vacancy [calculated using Eq. (9)] are shown in Fig. 6(a). For a single H atom in the vacancy, the MTP prediction of –0.57 eV is in excellent agreement with our DFT value of –0.58 eV, and well within the range of previous DFT and experimental data [94,101,102]. The segregation energies of the second, third, and sixth H atoms are also predicted accurately. However, those of the fourth and fifth H atom differ significantly from the corresponding

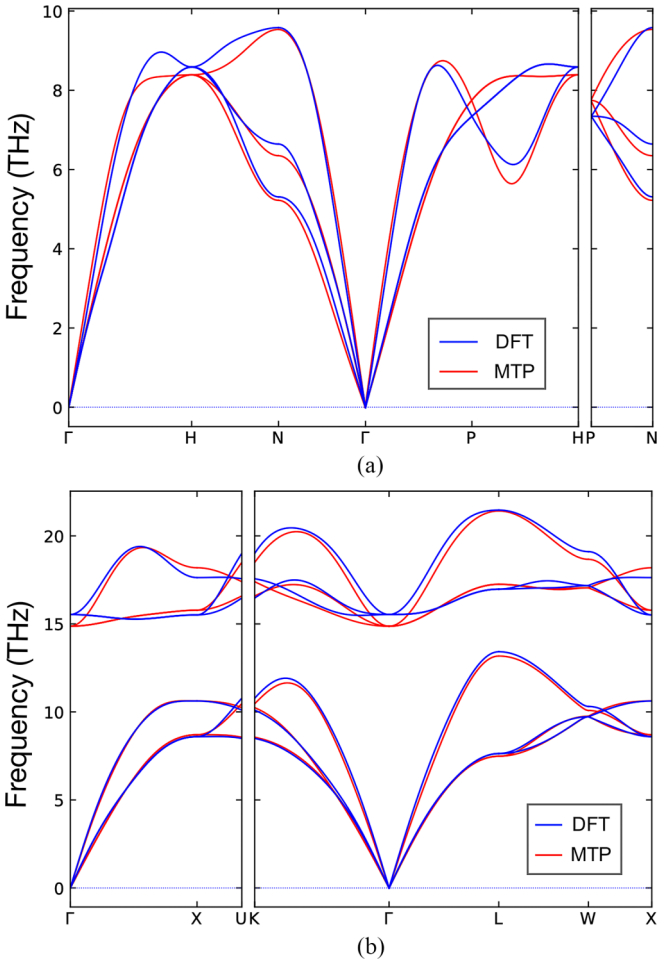


FIG. 4. Phonon dispersion spectra of (a) Fe and (b) TiC.

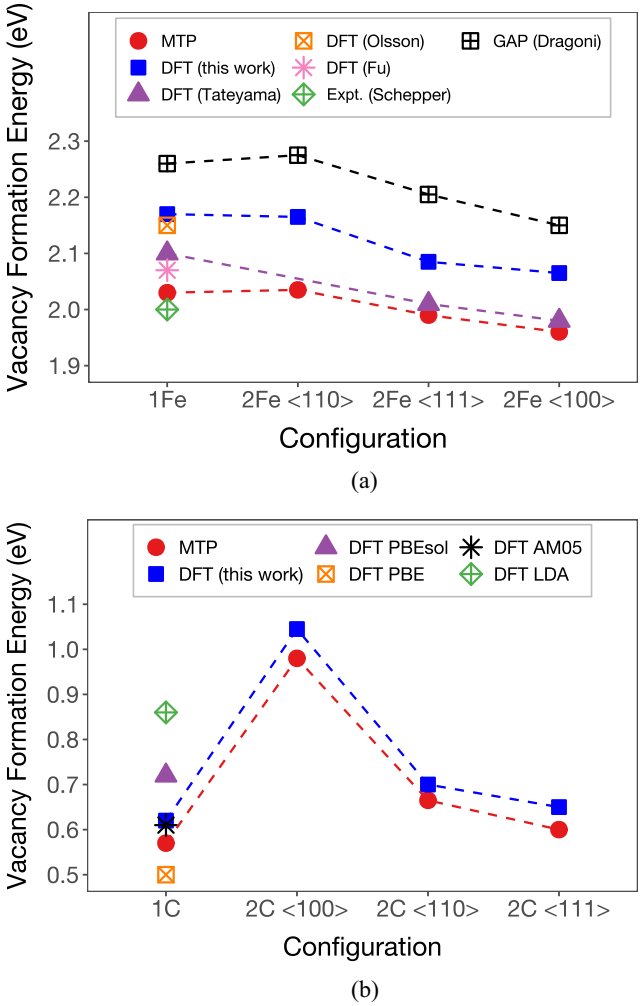
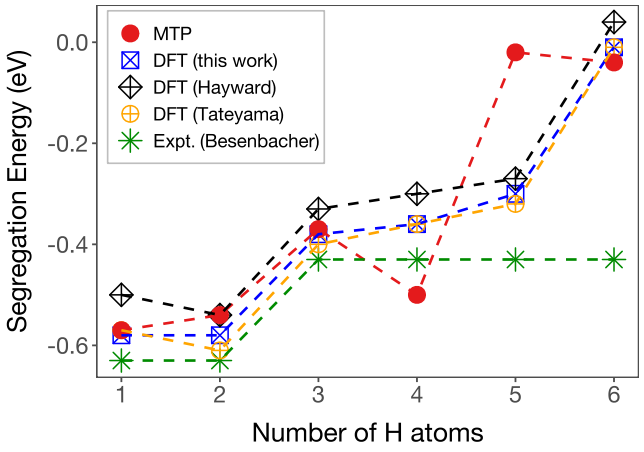
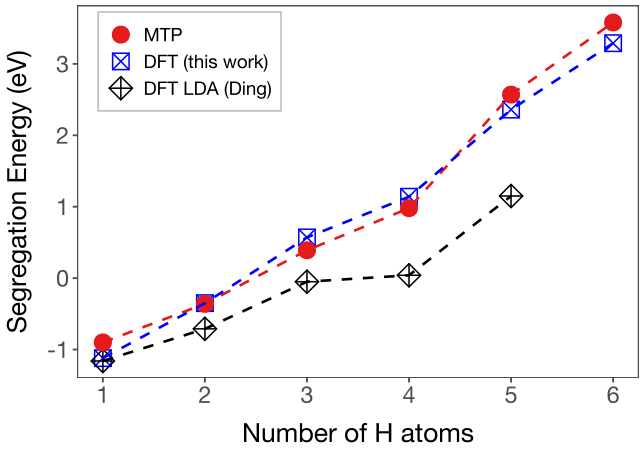


FIG. 5. Vacancy and divacancy formation energies predicted by MTP in (a) Fe and (b) TiC. The divacancy formation energies are reported *per vacancy* in the pair. Data from Tateyama and Ohno [94], Olsson *et al.* [95], Fu *et al.* [98], Schepper *et al.* [96], Dragoni *et al.* [66], and Råsander *et al.* [97] are also shown.



(a)



(b)

FIG. 6. Incremental segregation energy of multiple H atoms trapped in (a) Fe vacancy in bcc Fe and (b) C vacancy in TiC. Experimental data from Besenbacher *et al*. [102] along with DFT results of Hayward *et al*. [101], Tateyama *et al*. [94], and Ding *et al*. [32] are also shown.

DFT values (errors of –0.15 eV and +0.28 eV, respectively). MTPs trained using a higher cutoff radius lead to consistent segregation energies; however, increasing the cutoff radius results in inferior elastic constants and interstitial H solubility in bcc Fe, among other properties [as shown in Fig. 23(b) in Appendix A]. This trade-off therefore reflects a limitation of the MTP. Since high H chemical potentials leading to the trapping of four or more H atoms in a single vacancy are not imposed in this study, this compromise is accepted.

Figure 6(b) shows the segregation energies of one to six H atoms in a C vacancy in TiC. For a single H atom, the MTP prediction of –0.90 eV rightly points to the far superior trapping in C vacancies, yet is higher than the corresponding DFT value by 0.22 eV. The segregation energy in C vacancy is also found to be sensitive to the MTP cutoff radius, as seen in Fig. 23(b) below, and lowering the cutoff radius may improve the MTP prediction further. However, since the energy is large in magnitude relative to other trap sites in Fe and TiC (as well as the TiC/Fe interface, as shown later), the energy difference of 0.22 eV does not alter the equilibrium H distribution and

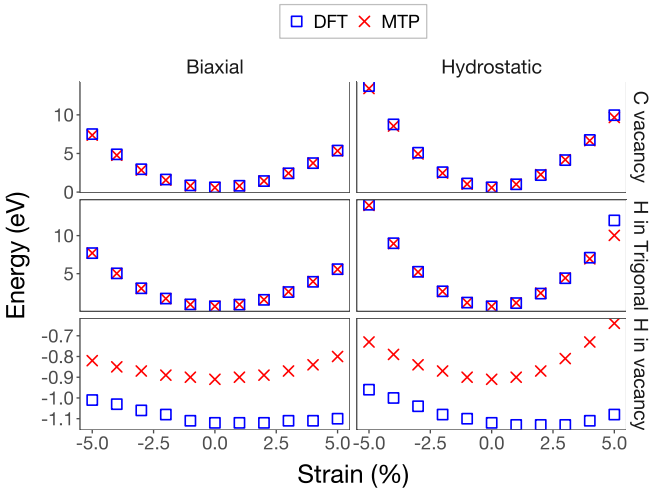


FIG. 7. Effect of strain on C vacancy formation energy and H segregation energy in trigonal and C vacancy sites in TiC.

kinetics significantly. The trends in incremental segregation energies of 2–6 H atoms obtained with MTP agree well with our DFT results. Previous calculations by Ding *et al*. using the LDA functional resulted in lower segregation energies [32], although the GGA functional used in this study is found to be better suited for TiC and similar compounds [103].

5. H solubility in strained Fe and TiC

Coherency strains prevalent at the interface can alter the H segregation and vacancy formation energies, which are both relevant to H trapping. The MTP is therefore benchmarked against DFT for strain-induced H solubility in Fe and TiC, along with C vacancy formation in TiC. As coherent TiC is usually plate- or disk-shaped with an incoherent side interface [34], a biaxial strain state is prevalent at the interface. However, in some instances, the side interface of these carbides can also form semicoherent structures [34], such that hydrostatic compressive strains in TiC may also be expected. Therefore, both biaxial and hydrostatic strains are considered. Strains are applied in the range of ±5%, and for the biaxial case, the unstrained dimension is allowed to relax with MTP. DFT energies are obtained in a single-point calculation performed on the MTP-relaxed configuration. Figure 7 shows the C vacancy formation energy (top panel), H solution enthalpy in a trigonal site, which is the preferred interstitial site for H (middle panel) and H segregation energy in a C vacancy (bottom panel) over the studied strain range. For C vacancy formation and H solution enthalpy in the trigonal site, an excellent agreement with DFT is obtained. MTP predictions of H segregation energies in C vacancies are higher by approximately 0.2 eV (which has been addressed in Sec. III B4), yet their variation with strain is in good agreement with DFT, especially in the compressive regime, which is most relevant, as the TiC sublattice is under compressive strain at the interface because of its larger lattice parameter.

For the Fe matrix, because of the anisotropic nature of the imposed biaxial strain, two previously identical tetrahedral and octahedral interstices become inequivalent, as shown in Fig. 8. The H solution enthalpy in these sites, calculated with

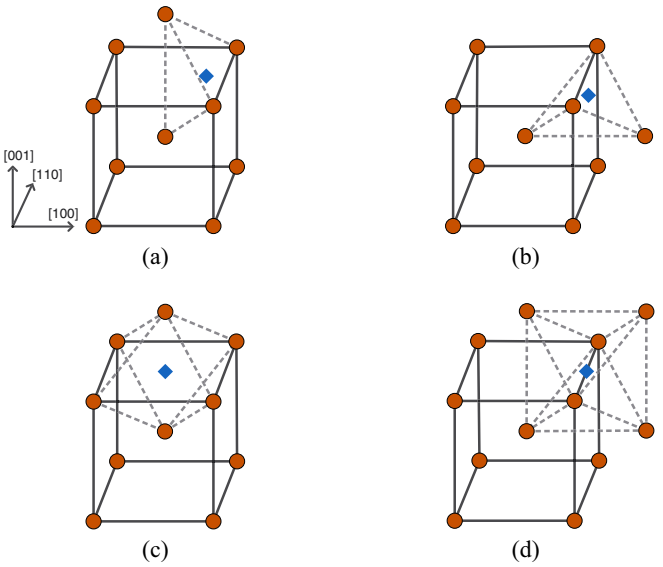


FIG. 8. Inequivalent interstitial sites in Fe under biaxial strain. Tetrahedral sites (a) T1 and (b) T2, and octahedral sites (c) O1 and (d) O2.

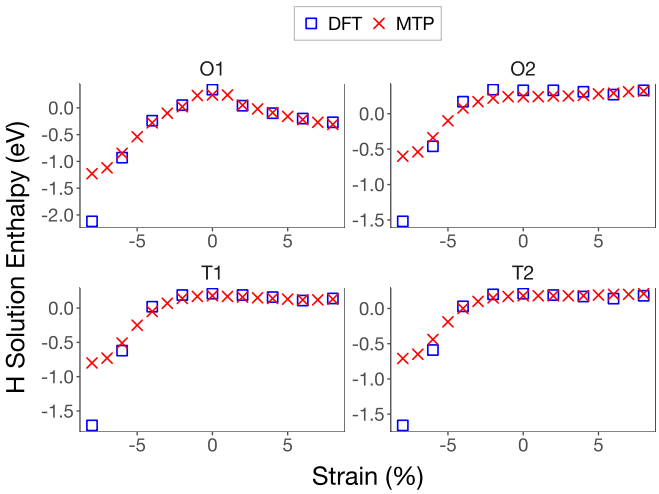


FIG. 9. H solution enthalpy in tetrahedral and octahedral interstices in Fe under biaxial strain applied along the [100] and [010] directions.

Eq. (6), is shown in Fig. 9. The MTP predictions for all sites are in good agreement with DFT in the tensile regime. Some significant differences between DFT and MTP are found at a compressive strain of –8%. However, because of the larger lattice constant of TiC, only tensile strains are expected in the Fe sublattice at the coherent interface.

6. Migration barriers

The energy barriers for the migration of H and/or vacancies in Fe and TiC found with MTP are listed in Table V. The migration of interstitial H between adjacent tetrahedral sites in bcc Fe is found to have an energy barrier of 0.08 eV with MTP, which is in close agreement with a previous DFT value of 0.09 eV [82]. Moreover, the migration barrier for an Fe vacancy to jump between nearest-neighbor sites is found to be 0.79 eV, which is higher than that reported in a previous DFT study by 0.12 eV [98]. Machine learning potentials designed specifically for Fe have demonstrated better accuracy in this regard [66].

In TiC, two different processes for the migration of H between trigonal sites are known [27]. In one of them, H remains bonded to the same C atom, but the C–H bond is rotated, such that the H atom moves into the nearest trigonal site. The barrier associated with this step is found to be 0.30 eV, which is in close agreement with DFT (0.29 eV) [27]. In a second process, the C–H bond is broken, and the H atom forms a new bond with the adjacent C atom. The characteristic barrier is found to be 0.42 eV, and agrees well with the DFT value of 0.47 eV [27].

For H migration between adjacent C vacancies, the energy barrier obtained with MTP is 0.89 eV, which is lower than previous DFT reports of 1.10 eV (GGA) [104] and 1.19 eV (LDA functional) [32]. This is consistent with the higher prediction of H segregation energy in the vacancy obtained with MTP, as discussed in the previous sections. As for the migration of the C vacancy itself, although the calculated values are higher than DFT values, the relative error is limited (6% compared to the result from [105]).

7. H diffusivity in bcc Fe

The diffusivity of H in bcc Fe calculated with MTP is shown in Fig. 10, and the corresponding activation energy and preexponential factor are listed in Table VI. The diffusion coefficient is in good agreement with previously reported data. The computed activation energy is found to be 0.061 eV,

TABLE V. Migration barriers in bcc Fe and TiC. In the table, "NN" stands for nearest-neighbor. Values are in eV.

Process	MTP	Literature
Fe		
H migration between tetrahedral sites	0.08	0.09 [82]
Fe vacancy migration	0.79	0.67 [98], 0.66 [66]
TiC		
H migration between 1NN trigonal sites	0.30	0.29 [27]
H migration between 2NN trigonal sites	0.42	0.47 [27]
H migration between adjacent C vacancies	0.89	1.19 [32]
C vacancy migration	4.10	3.85 [105], 3.46 [68]

TABLE VI. Activation energy and preexponential factor for H diffusivity in bcc Fe.

Property	MTP	MD	Expt.
Activation energy (eV)	0.061	0.056 [106]	0.068 [107], 0.046 [109], 0.040 [108]
Preexponential factor (10^{-8} m^2/s)	4.90	4.35 [106]	5.8 [109], 4.2 [108]

close to the value of 0.056 eV obtained with an Fe–H EAM potential [106], and within the range of reported experimental values [107–109]. The preexponential factor D_0 is found to be 4.90×10^{-8} m^2/s, which also falls within the range of experimental values [108,109] and agrees well with the value of 4.35×10^{-8} m^2/s obtained with the EAM potential [106].

8. H diffusivity in TiC

H diffusivity in TiC obtained with MTP is shown in Fig. 11. The corresponding activation energy is found to be 0.265 eV, and although literature data are lacking, the value is close to the H migration barrier of 0.29 eV between adjacent trigonal sites found with DFT [27] (the corresponding MTP value is 0.30 eV, see Table V). The preexponential factor is 1.10×10^{-7} m^2/s, and H diffusivity is up to three orders of magnitude lower than that in bcc Fe.

C. Benchmark properties of coherent TiC/Fe interface

1. Fundamental properties

The crystal structure of the coherent TiC/Fe interface is shown in Fig. 1(a). The two phases have a common lattice parameter (in the interface plane), and the lattice mismatch between Fe and TiC is accommodated by the elastic coherency strains. The interface energy, common lattice parameter, and the Fe–C distance normal to the interface plane are crucial properties governing the atomic structure of the interface. A comparison of the MTP values with relevant DFT data from literature is presented in Table VII. MTP predictions of these properties are found to be in excellent agreement with DFT values.

2. Vacancy formation energies

The formation energies of various vacancy configurations at the interface are shown in Fig. 12. The studied configurations include an isolated Fe or C vacancy, Fe or C divacancies, as well as a nearest-neighbor Fe–C vacancy pair. The MTP predictions are in excellent agreement with our DFT results. The formation energies of various SIA configurations at the coherent interface have also been provided in Appendix C.

3. H segregation at the coherent interface

Several DFT studies have examined H segregation at the coherent interface between Fe and TiC [27,30,31,60]. Various interstitial sites with preferential H segregation have been found in the Fe sublattice, which differ in either the local chemical environment or the strain state (because of the anisotropic coherency strains). These sites are shown in Fig. 13. Sites O1, T1, and T4 lie on the interface plane and are coordinated by atoms from both phases—O1 has an octahedral coordination, formed between five Fe atoms and one Ti atom, T1 is tetrahedral-like, formed between three Fe and one Ti atom, and T4 lies at the centroid of the triangle formed by two Fe and one Ti atom. Sites T2 and T3 are tetrahedral-like sites coordinated by Fe atoms only and differ in the strain state of the tetrahedron. Additionally, sites V1 and V2 refer to C vacancies at the interface layer and the subsequent layer (along the interface normal direction), respectively.

The H segregation energies at these sites as calculated with MTP are shown in Fig. 14. For the interstitial sites, MTP predicts the correct site preferences, although the segregation energies are consistently higher than their DFT counterparts. T2 is found to be the most favorable, in agreement with previous DFT reports [27,30,31,60]. The H segregation energy of –0.19 eV is higher than our DFT value of –0.29 eV by 0.1 eV. Overall, the maximum difference between MTP and DFT

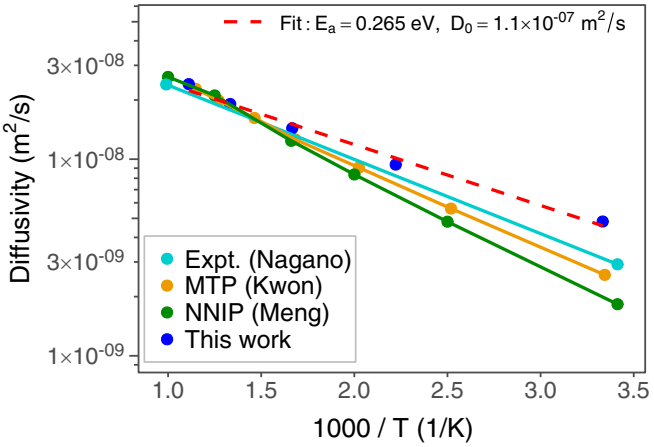


FIG. 10. H diffusivity in bcc Fe. Reference data are taken from [67], [110], and [108].

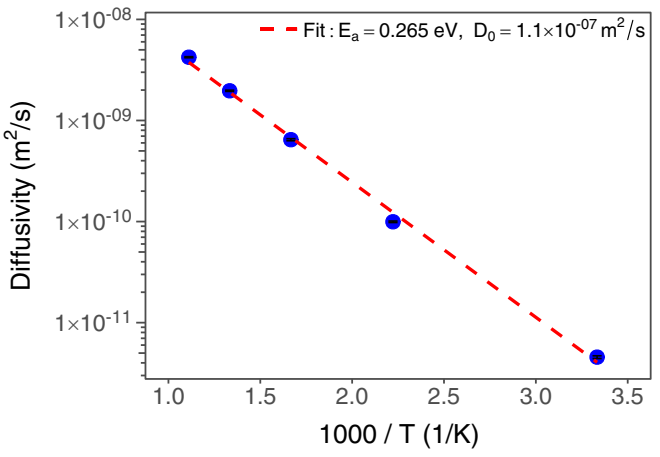


FIG. 11. H diffusivity in TiC.

TABLE VII. MTP prediction of coherent interface properties namely, the interface energy, the common lattice parameter and the Fe–C distance normal to the interface plane.

Property	MTP	Literature (DFT)
Interface Energy (eV/Å^2)	0.014	0.012 [88], 0.014 [71], 0.016 [111], 0.024 [70]
Lattice parameter (Å)	3.03	3.04 [27], 3.00 [88], 2.99 [70], 3.03 [111]
Fe-C distance (Å)	1.89	1.91 [27], 1.88 [88], 1.88 [71], 1.90 [111]

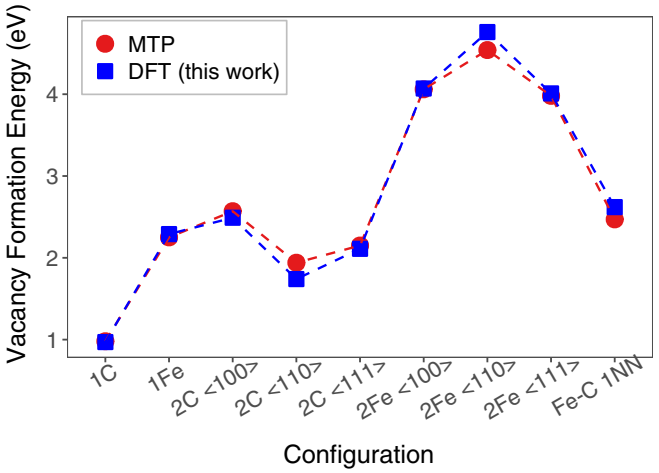


FIG. 12. Various vacancy formation energies at the coherent interface.

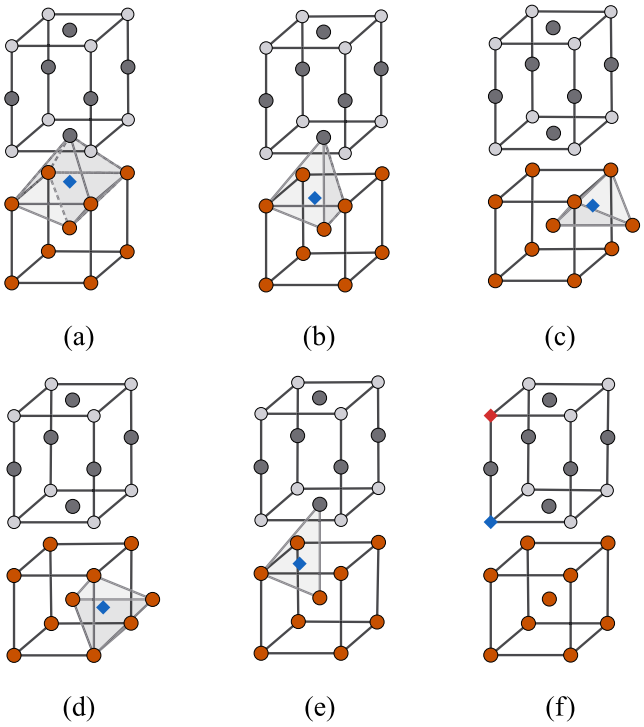


FIG. 13. Schematics of various H segregation sites at the coherent interface. (a) Octahedral site O1, tetrahedral sites (b) T1, (c) T2, and (d) T3, (e) triangular site T4, and (f) vacancy sites V1 and V2, marked in blue and red, respectively.

values is 0.14 eV, at site T1. Experimental reports of segregation energies attribute a value between –0.18 eV and –0.6 eV to the coherent interface [45], the lower limit of which corresponds well with the DFT and MTP data. Comparing the prediction for C vacancies, at V1, the MTP value is higher than DFT by 0.2 eV. The same deviation was seen for H segregation in C vacancies in bulk TiC as discussed previously (Sec. III B4). At V2, the MTP and DFT values are much closer, although opposite trends are seen for the site preference between V1 and V2. Nevertheless, the H segregation energies at interface vacancies are found to be similar to or even slightly higher than those in bulk vacancies, in agreement with previous DFT studies [29,30].

4. Summary of MTP benchmarking

In summary, we have shown that the MTP can predict the elastic and dynamic properties, vacancy formation energies, H solubilities, migration barriers (for both H and vacancy), and H diffusivities in both bulk phases, as well as the interface energy and atomic relaxation around the coherent TiC/Fe interface, and the corresponding vacancy formation energies and H segregation energies with DFT accuracy. Additionally, the MTP can also predict the correct bond length of H_2, at 0.75 Å, in agreement with our DFT calculations. With this potential at hand, we proceed to investigate the atomic structure and H trapping characteristics of the different interfaces.

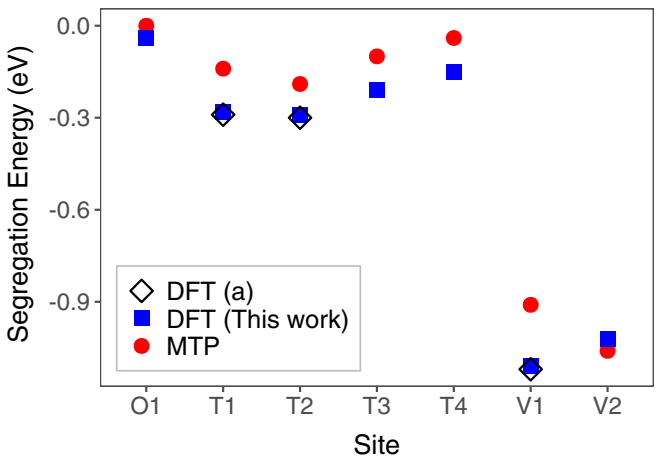


FIG. 14. Segregation energy of H at various sites at the coherent interface. DFT data labeled as (a) is taken from the work of Zhang *et al.* [29].

D. Application of the Fe–TiC–H MTP IAP

The MTP is applied to study the energetics of hydrogen in TiC precipitates with different interface characters. Results of relaxed atomic structures and H segregation energies and migration barriers at the coherent, semicoherent, and incoherent TiC/Fe interfaces as investigated with MS simulations are presented below.

1. Reassessing the coherent interface

In DFT calculations of the coherent TiC/Fe interface, most of the mismatch strain is found to be accommodated by the expansion of the Fe matrix, which is significantly more compliant than TiC [29,30]. However, the common lattice parameter also depends on the volume fraction of the precipitate [112–114], but the supercell used in DFT calculations comprises approximately 40% TiC [29,30], whereas experimental TiC volume fractions are below 1% [115]. For modeling such low TiC volumes, many more Fe atoms would be needed, which makes DFT computationally prohibitive. The MTP is used to study the change in lattice parameter and H segregation energy as a function of TiC volume fraction ranging from 3% to 40%. The supercells are created by employing the same number of TiC layers as in the DFT supercell [shown in Fig. 1(b)] and increasing the number of Fe layers along the interface normal direction.

The in-plane common lattice parameter as a function of the volume fraction of TiC is shown in Fig. 15(a). For the highest TiC volume fraction, a value of 3.02 Å is obtained, which is well within the range of reported DFT values from 2.99 Å to 3.04 Å [27,70,71,116]. As the volume fraction of TiC decreases, the common lattice parameter moves towards that of Fe, in agreement with the continuum theory of inclusions [112–114], reaching a value of 2.86 Å at 3% TiC. This leads to coherency strains at the interface that are significantly different from the DFT calculations, which can in turn affect H segregation.

The variation in H segregation energy at the two most preferred sites at the coherent interface, T1 and T2 [shown in Figs. 13(b) and 13(c)], with the common lattice parameter is shown in Fig. 15(b). At T2, the H segregation energy increases linearly with decreasing lattice parameter, and approaches that in bulk Fe [0 eV according to Eq . (7)] in the dilute limit. In contrast, the segregation energy at T1 reaches a maximum at 2.94 Å, beyond which it decreases, such that the site preference changes from T2 to T1. Differing trends in T1 and T2 originate from the coordination of the first-neighbor shell at these sites—while T2 is coordinated by four Fe atoms that align with the interface plane (and the enclosed volume is therefore directly proportional to the lattice parameter), an Fe–Ti pair in the first-coordination shell of T1 is aligned normal to the interface plane, and can relax freely in response to the imposed strain.

The lowest H segregation energy at the coherent interface for a lattice parameter of 2.86 Å (TiC volume fraction of 3%) is found to be –0.13 eV, at T1. For comparison, the same that obtained from DFT calculations (TiC volume fraction of 40%) is –0.19 eV, at T2. Although the segregation energy does not differ significantly in this case, the changed site preference suggests the importance of capturing the elastic strain in the interface models accurately.

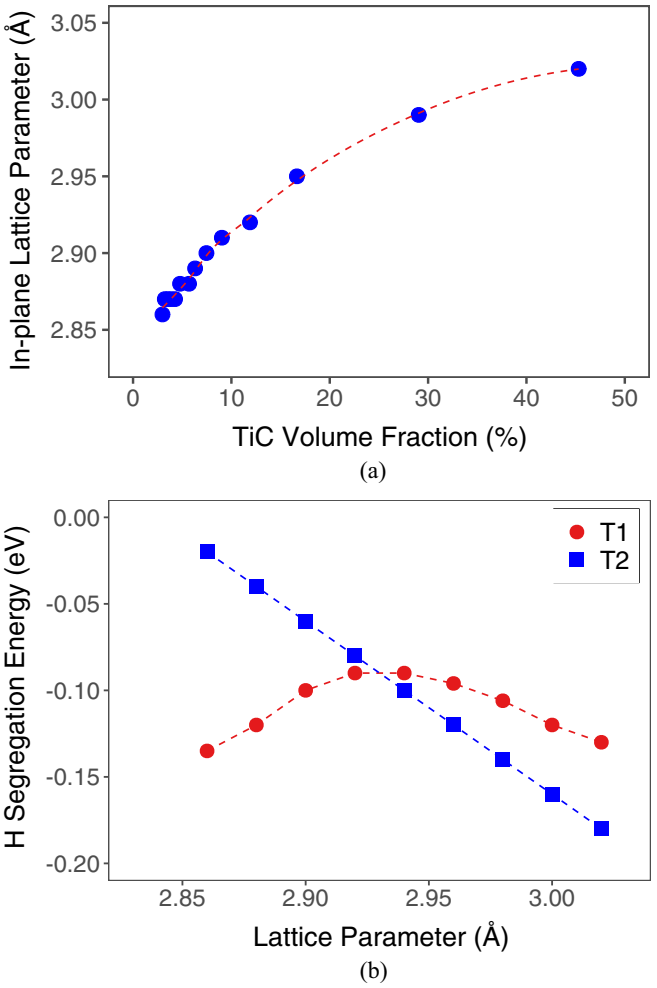


FIG. 15. Dependence of H segregation energy on supercell size. (a) The in-plane common lattice parameter of coherent TiC/Fe in the interface plane at different TiC volume fractions. (b) H segregation energy as a function of the common lattice parameter.

2. Semicoherent TiC

The elastic energy needed to accommodate the lattice mismatch between the carbide and the matrix becomes prohibitively large for TiC inclusions larger than a critical size (reported values range from 3 to 8 nm [36,37,117,118]). In such cases, the high tensile stresses in the Fe matrix are relieved by the formation of periodically arranged misfit dislocations at the interface, which then separate the coherent regions. Models of the semicoherent interface are created by stacking $n \times n \times n_Z$ TiC unit cells on top of $(n+1) \times (n+1) \times n'_Z$ Fe unit cells, where n is the number of in-plane repeating unit cells of TiC, and n_Z and n'_Z are the number of repeating TiC and Fe unit cells, respectively, out of the interface plane. By having an additional Fe unit cell along each of the two in-plane interface directions, two perpendicular misfit dislocations, with their glide planes coincident with the interface, are generated in the Fe matrix (one with Burgers vector along $[100]_{Fe}$, the other along $[010]_{Fe}$).

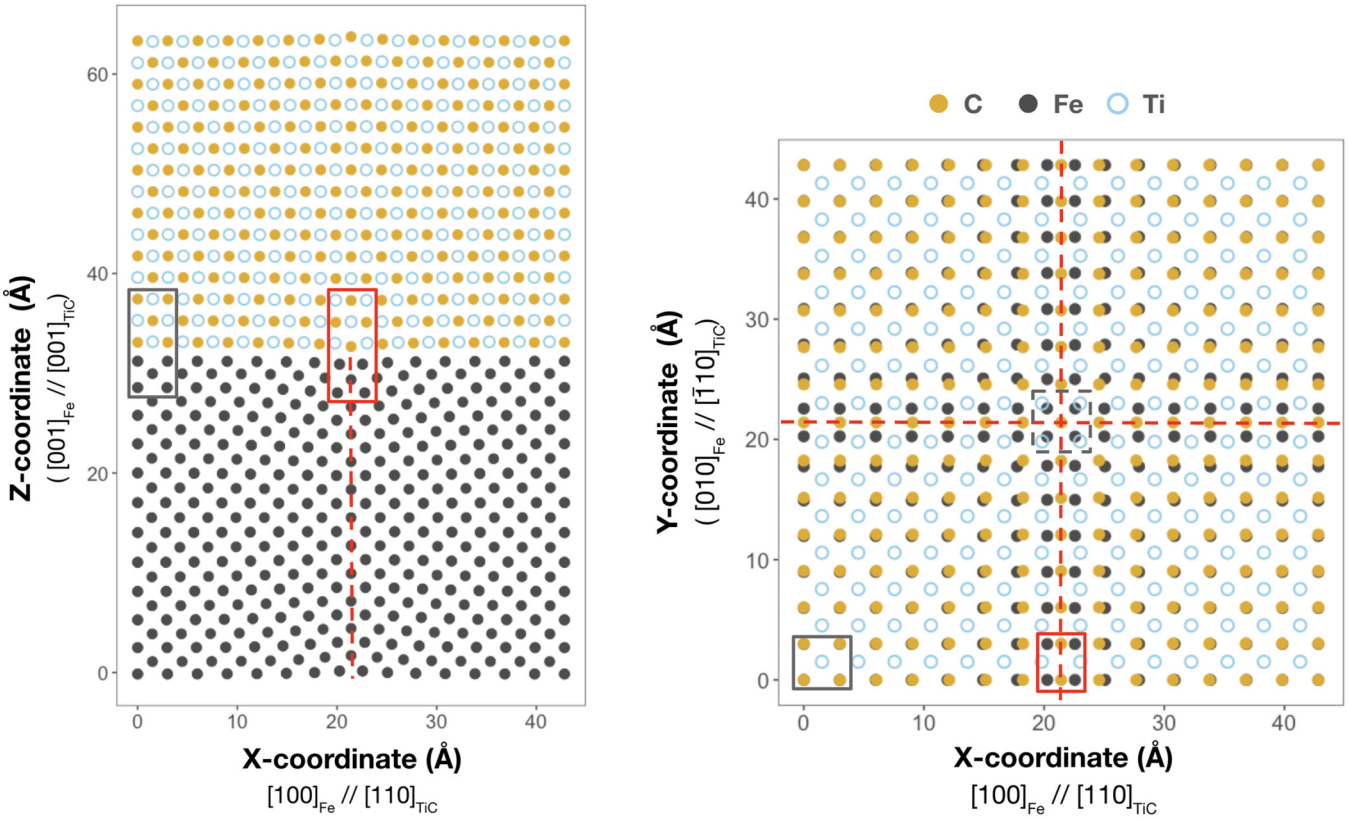


FIG. 16. Relaxed atomic structure of the semicoherent interface. (a) (010) plane. Only the first two atomic layers in the y direction are shown for clarity (b) (001 plane). Only the first Fe and TiC layers adjacent to the interface plane are shown for clarity. Yellow and black solid circles represent C and Fe atoms, respectively, while blue open circles represent Ti atoms. Coherent-like TiC/Fe units, where Fe atoms are aligned with C atoms across the interface, are marked with black solid lines. The extra half plane of Fe is marked with a red dashed line. The TiC/Fe unit cell containing the misfit dislocation is marked with red solid lines. Black dashed lines mark the TiC/Fe unit cell containing the intersection of misfit dislocations.

The minimum lattice mismatch between Fe and TiC [calculated as $|(n+1) \times a_{Fe} - n \times a_{TiC}|$] is obtained for $n = 14$. The relaxed atomic structure of the corresponding semicoherent interface model is shown in Fig. 16 (atomic positions and lattice vectors are allowed to relax during minimization). Figure 16(a) shows the broad faces of the cuboidal TiC, where the extra half Fe atomic plane forming the misfit dislocation lies in the center (marked with red dashed lines). A TiC/Fe unit cell far from the misfit dislocation (marked with black lines) has near-perfect alignment of the Fe and C atoms, resembling the atomic structure of the ground state of the coherent interface. At the core of the misfit dislocation, a C atom lies exactly in between two Fe atoms (unit cell marked with red lines), and resembles the atomic environment of the misfit-dislocation core in DFT supercells of the semicoherent interface [27,31]. In Fig. 16(b), the atomic structure of the interface plane (only one Fe and TiC layer on either side of the interface plane) is shown. The two perpendicular misfit dislocations intersect in the center of the interface plane. The TiC/Fe unit cell around the intersection of dislocations comprises a C atom surrounded by four Fe atoms (marked with black dashed lines). This resembles the atomic environment of misfit intersection in DFT supercells [27,31]. These three distinct unit cells capture all the electronically distinct regions of the semicoherent interface.

The atom positions and interatomic distances around the core of a misfit dislocation are shown in more detail in Fig. 17. The Fe–Fe spacing in the unit cell containing the dislocation core and that in the adjacent one is found to be 2.31 Å and 2.51 Å, respectively, while the corresponding C–C spacing is 3.18 Å. Within three unit cells from the core, both Fe–Fe and

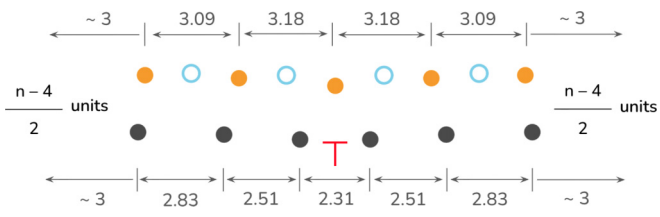


FIG. 17. The lattice spacing around the misfit-dislocation core (in Å) parallel to the interface plane. The position of the extra half plane of Fe is also depicted in red. Note that the dislocation glide plane lies in the Fe layer below the one shown here. The strain and width of the misfit region are independent of the size n of the supercell, and only affect the number and width of coherent units.

C–C spacings reach a value of approximately 3 Å, indicating coherency between Fe and TiC. In the DFT studies of the misfit-dislocation core, although the chemical environment turns out to be equivalent to our model, the Fe–Fe spacing (or C–C spacing, which are equal by design in these models) is reported to be 3.10 Å [27]. Moreover, the Fe–C distance across the interface measured along the [001] direction in our model is found to be 1.78 Å, different from the DFT results of Lu *et al*. [71] (1.59 Å) and Di Stefano *et al*. [27] (1.65 Å).

DFT calculations of the intersection region of the perpendicular misfit dislocations [marked with black dashed lines in Fig. 16(b)] similarly fail to capture the atomic relaxations accurately. The in-plane Fe–Fe distance in our model is found to be 2.34 Å, much lower than the DFT calculated value of 3.01 Å of Di Stefano *et al*. [27]. Further, the Fe–Ti distance across the interface is found to be 2.54 Å with MTP, as opposed to DFT reports of 2.88 Å [27] and 2.80 Å [71]. For both the dislocation-core and intersection regions, MTP values of the Fe–C and Fe–Ti distances are in fact similar to those found in the first-principles calculations of Sawada *et al*., who use a single, large supercell similar to our study, but alleviate the computational cost by using the $O(N)$ Krylov-subspace method in their calculations [118].

The atomic structure of the semicoherent interface is found to be independent of the number of TiC units n. Several models, with n ranging from 8 to 16, lead to the same atomic spacings at the misfit-dislocation core and intersection regions, and only affect the width (or number of units) of the coherent region, as indicated schematically in Fig. 17.[2] The number of Fe and TiC units along the interface-normal direction, n'_Z and n_Z (11 and 7, respectively), is chosen to be sufficiently large to ensure negligible interaction between the interface and its periodic image, and converged interface energies. Moreover, unlike the fully coherent TiC models discussed in the previous section, decreasing the TiC volume fraction does not have any effect on the in-plane lattice parameter, as the elastic strain from the lattice mismatch between $n+1$ Fe and n TiC unit cells is significantly smaller compared to that in the 1:1 case for the same TiC volume.

Next, the H segregation energy at the semicoherent interface is investigated. The distinct local atomic environments and the corresponding strain field can lead to a wide range of possible trapping sites and H solubilities. Similar to the coherent interface, these sites are identified as possible interstitial sites in the Fe and TiC sublattices adjacent to the interface plane. The H segregation energy map in interstitial sites across the interface plane is shown in Fig. 18. In the coherent regions, tetrahedral site T2 is found to be the most stable with a segregation energy of –0.16 eV. H dissolution in T1 is also exothermic, with a segregation energy of –0.12 eV (refer to Fig. 13 for schematics of these sites).

Moving towards the misfit region, as the in-plane Fe–Fe spacing decreases to 2.83 Å three unit cells away from the

[2]For odd n, i.e., even number of Fe unit cells, the dislocation is no longer in the center of the simulation cell and thus, not equidistant from its periodic images. The interatomic distances around the core, however, are not affected owing to the sufficiently large supercell size.

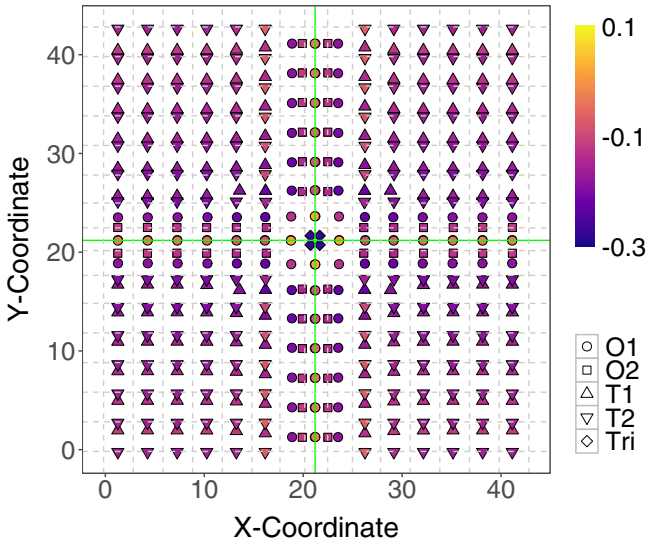


FIG. 18. H segregation energy (in eV) on the interface plane. Dislocation lines are indicated in green. The grid spacing reflects the Fe lattice spacing on the interface layer.

dislocation core, T1 becomes more favorable for H than T2. The segregation energy at this site decreases to –0.16 eV, while that at T2 increases to –0.06 eV. Adjacent to the misfit-dislocation core, where the Fe lattice spacing is 2.51 Å, both T1 and T2 become unfavorable for H as the segregation energy becomes positive. The octahedral site O1 [Fig. 13(a)], however, is exothermic for H dissolution, with a segregation energy of –0.18 eV. In the unit cell containing the misfit-dislocation core, the only interstitial site with exothermic H dissolution is an octahedral site O2, with a segregation energy of –0.11 eV. This site, shown schematically in Fig. 19(a), is formed on the top edge of the Fe lattice, directly above a Ti atom. The same site is reported to have a segregation energy of –0.20 eV in the DFT calculations of H segregation at a misfit dislocation [27]. However, the authors also found a tetrahedral site (similar to T1) to be most favorable, with a segregation

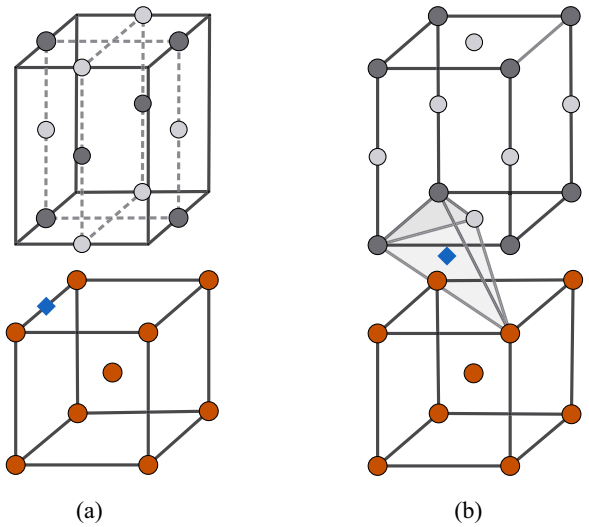


FIG. 19. Schematics of additional H trapping sites at the semicoherent interface. (a) O2 and (b) Tri.

energy of –0.49 eV, which is in contradiction to our findings. As discussed above, the high in-plane compression of the Fe matrix around the misfit dislocation is not captured correctly in DFT calculations because of the constraints on supercell size.

Considering the sites around the intersection of misfit dislocations, the variation in site preference with the distance from a dislocation core remains the same, although the corresponding H segregation energies are lowered slightly. The segregation energy at T2 decreases to a minimum of –0.20 eV, while that at T1 and O1 reaches –0.22 eV. In the unit cell comprising the intersection of dislocations, trigonal sites (labelled Tri), lying between two Ti and one Fe atom in the (111) planes, have the lowest segregation energy of –0.27 eV. This site is shown schematically in Fig. 19(b) and is the deepest (interstitial) trap site at the interface. This is also the only stable site where H lies between the Fe and TiC layers at the interface, rather than on the Fe layer. Similar sites are also reported to be the most preferred in DFT calculations of the misfit-dislocation intersection region; however, the segregation energies of approximately –0.50 eV are significantly lower than those found with MTP [27,31].

3. Side interface

The aforementioned models of the semicoherent interface, although insightful for the broad TiC/Fe interface, are semiinfinite, as they are unbound in the x and y directions. However, in reality, the carbides are embedded inside the Fe matrix, and thus also have a distinct side interface. The side interface is reported to be semicoherent up to a thickness of only 0.87 nm, and is generally incoherent [34,36,37]. For studying the side interface with MTP, a coherent TiC particle of dimensions 1.5 nm × 1.5 nm × 1.8 nm is embedded in a Fe matrix following the Baker–Nutting orientation along the two equal sides. The atomic structure of the side interface is therefore constrained by the orientation of the broad interfaces. Figure 20 shows a cross section of the relaxed atomic structure of the side interface, as obtained with MTP. The side interface is seen to be incoherent, with some local atomic configurations resembling the intersecting misfit dislocations (marked with red dashed lines). Moreover, the atomic strains are randomly oriented, with both compressive and tensile regions in proximity, without any periodicity.

H segregation sites are identified in a manner similar to that at the coherent and semicoherent interfaces, although they are not as well defined because of the largely distorted atomic structure of the interface. The most stable sites for H are tetrahedral-like, in the tensile regions of the side interface, with a segregation energy of −0.12 eV. This result agrees well with a previous DFT study of an incoherent $(001)_{Fe}//(001)_{TiC}$ interface, where segregation energies were found to range from –0.20 to –0.10 eV [27]. Several other model sizes are also tested in our work by increasing the number of TiC layers along the z axis, yet the segregation energies are found to vary only within a very narrow range.

4. Carbon vacancies

In fully coherent TiC, the C vacancy formation energy at the interface is higher than that in bulk TiC [30]. In

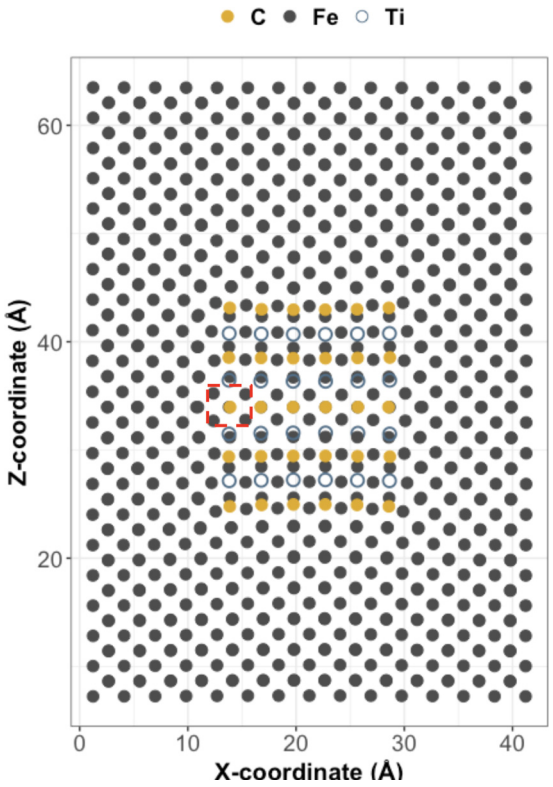


FIG. 20. Cross section of the embedded TiC showing the relaxed atomic positions at the side interface. Fe–C atomic coordination resembling that of perpendicular misfit dislocations is marked with red dashed lines.

semicoherent TiC, tensile strains are expected in TiC near the misfit dislocations, where the C–C lattice spacing is found to be 3.18 Å, as shown in Fig. 17. The volumetric strain in the C sublattice at the interface plane is shown in Fig. 21(a). While there is negligible strain in the coherent regions, that above the misfit-dislocation and the dislocation-intersection region is more pronounced. Tensile strains are known to enhance the formation of C vacancies in κ carbides [119]. To explore a similar phenomenon in TiC, the C vacancy formation energy in the interfacial C sublattice is calculated with MTP. Figure 21(b) shows the vacancy formation energy and corresponding H segregation energy along the broad face of interfacial TiC (moving from left to right along the bottommost C layer in Fig. 21(a), such that the misfit-dislocation core lies at $x = 21.2$ Å). In the coherent regions, the C vacancy formation energy is 0.86 eV, similar to that obtained with DFT for the coherent interface model [30]. However, a C vacancy at the misfit core is found to have a lower formation energy of 0.62 eV. The H segregation energies at the C vacancies along the broad face, however, do not vary significantly from those in the coherent regions to to those at the misfit dislocation.

Next, the C vacancy formation energy above a dislocation line is shown in Fig. 21(c) (moving from left to right along the middle C layer in the middle of Fig. 21(a), such that the perpendicular misfit dislocations intersect at $x = 21.2$ Å). Beginning at 0.62 eV, the vacancy formation energy is lowered even further, and drops considerably to a minimum of 0.07 eV directly above the intersection point of the dislocations.

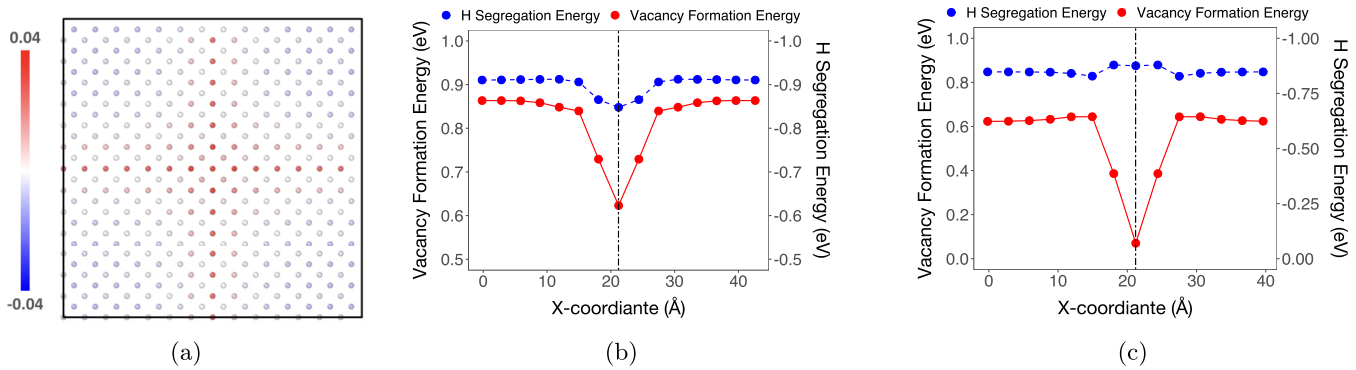


FIG. 21. Strain-induced vacancy formation and H segregation at the semicoherent interface. (a) Volumetric strain in the C sublattice at the interface layer. C vacancy formation and corresponding H segregation energies (b) across the breadth of the semicoherent TiC, with the misfit dislocation in the center at $x = 21.2$ Å (shown in black center line), and (c) along a dislocation line, where the two perpendicular dislocations intersect at $x = 21.2$ Å

However, the H segregation energy at this vacancy is also relatively similar to that at other vacancy locations.

Finally, the vacancy formation and corresponding H segregation energies at various locations along the incoherent side interface of TiC are calculated. A precise determination of their dependence on the local environment is challenging owing to a lack of well-defined periodicity at the interface. However, the vacancy formation energy is found to be highly sensitive to the local atomic arrangement and atomic strains. The cross section of the side interface, as shown in Fig. 20, has alternating C and Ti layers along the edges of the cubic TiC. In layers where the C atoms are adjacent to Fe, the vacancy formation energies are found to be exothermic, and vary between –0.01 and –1.02 eV depending on the Fe–C distance and the local strains. Simultaneously, in TiC layers where a Ti atom is adjacent to Fe at the edge, the C vacancy formation energy can be much higher than in the bulk, ranging between 0.16 and 1.61 eV.

The H segregation energies at these vacancies at the side interface are also found to be sensitive to the location of the vacancy, in contrast to those at the coherent and semicoherent interfaces. Segregation energies in the range –1.59 eV to –0.44 eV are found; however, lower energies correspond to vacancies with higher formation energies, where the presence of a vacancy would be more improbable. C onsidering only the exothermically formed vacancies, the segregation energies are between –0.44 eV and –0.69 eV.

5. H migration in semicoherent TiC

To be able to populate the deep traps (i.e., C vacancies) with H, the activation energy for H migration into the vacancies must be sufficiently low. In the case where vacancies are present at the interface, the H migration barriers between stable interstitial sites in the Fe layer and the nearest C vacancies, as calculated with MTP, are found to be 0.18 eV, 0.06 eV, and 0.02 eV in the coherent, misfit-dislocation core, and dislocation-intersection regions, respectively. For comparison, the characteristic barrier for H migration in bcc Fe is 0.09 eV. Thus, H trapping in interface vacancies is energetically feasible, especially near the misfit dislocations.

From the interface, for H to migrate further into the bulk of TiC can be challenging, as previous DFT studies report a migration barrier of 1.19 eV between adjacent C vacancies in bulk TiC [27,32], while the corresponding value obtained with MTP is 0.89 eV. The H migration barrier between an interface vacancy and one in the subsequent layer in different regions of the semicoherent TiC, as calculated with MTP is shown in Fig. 22 [for reference, the two vacancy sites at the coherent interface are depicted in Fig. 13(f)].

The highest barrier is found in the coherent region, with a value of 0.62 eV, considerably lower than that in bulk TiC. The barrier is lowered further to 0.39 eV for vacancies lying above the misfit dislocation, and to 0.31 eV for vacancies above the intersection of the two perpendicular dislocations. Thus, the strain fields of misfit dislocations are likely paths for the ingress of H into bulk vacancies.

IV. DISCUSSION

The results above demonstrate that the finite-size constraints inherent to DFT supercells can significantly affect both the atomic structure and H segregation profiles at

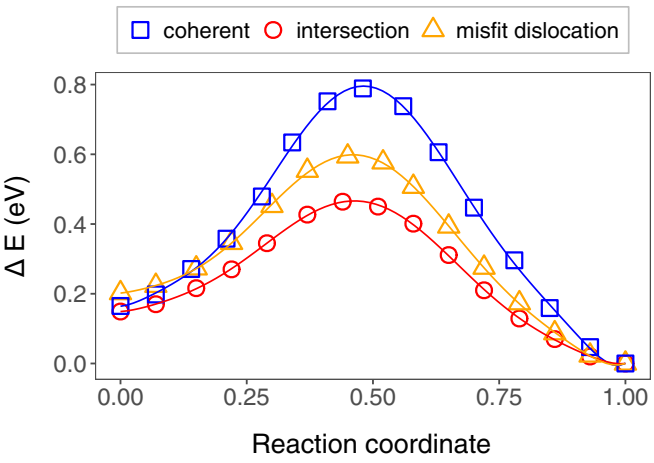


FIG. 22. H migration barrier from interface C vacancy to one in the subsequent layer in different regions of a semicoherent TiC.

semicoherent TiC/Fe interfaces, especially around misfit dislocations. This raises questions about the reliability of previously reported DFT results for segregation energies, where such supercell sizes were necessarily employed. The uncertainty quantification provided in Appendix D confirms that the MTP predictions for the semicoherent interface are within the interpolation regime, lending confidence to the results presented here.

Comparison with experimental data

In experimental analysis of H trapping with TDS, the amount and rate of H desorbing from a charged sample are recorded over a range of temperatures, from which the desorption activation energy is derived. The samples are generally processed through specific tempering conditions in order to control the precipitate sizes and elucidate the effect of coherency on trap strength. The measured activation energy in TDS thus corresponds to H desorption rather than H segregation. Considering that the precipitate is located in the interior of the sample, a desorbed H atom also passes through the Fe matrix (when trapped at the interface) and the TiC bulk (when trapped inside the carbide) to completely desorb from the sample. Thus, the experimental desorption activation energy is equivalent to the sum of the H segregation energy E^i_{seg} calculated in this work, and the energy barrier ΔE^i for H migration out of the trap into an interstitial site in the Fe matrix (H is assumed to desorb via interstitial sites in the matrix because of the large volume of the matrix compared to the carbide), the H migration barrier ΔE^{Fe} in the Fe matrix (0.09 eV), and the H migration barrier ΔE^{TiC} in TiC (0.47 eV) if H is trapped in the bulk of TiC. The so-defined activation energy for desorption is represented as

$$E_{des} = -E^i_{seg} + \Delta E^i + \Delta E^{Fe} + \Delta E^{TiC}, \qquad (10)$$

where the term ΔE^{TiC} is applicable only for trap sites in the bulk of the carbide. For ΔE^i, if the trap is an interstitial site at the interface, then the barrier for H to migrate from the strained interface sites to tetrahedral interstices in the pristine Fe matrix is assumed to be zero for simplicity, although a small but finite strain-induced barrier may exist. If trapping occurs at interface vacancies, then the corresponding barriers are 0.18 eV, 0.06 eV, and 0.02 eV in coherent, misfit-dislocation core, and dislocation-intersection regions, respectively. For the incoherent vacancies, ΔE^i is not well known, and therefore has not been applied in the determination of E_{des}. The MTP-obtained desorption activation energies are listed in Table VIII and addressed in the following discussion.

TDS measurements on ferritic steels containing TiC particles yield multiple activation energies in the range 0.4 eV–1.5 eV, corresponding to various trap sites at the interface and in bulk TiC [17,22,34,40–42,45]. Fully coherent TiC/Fe interfaces are reported to have an activation energy between 0.43 eV and 0.61 eV [17,41], depending on the tempering conditions, while the corresponding DFT values range from 0.2 to 0.3 eV [27,30,31]. It is noteworthy that the determination of the activation energy with TDS is based on specific assumptions, such as the absence of re-trapping once the hydrogen atom is desorbed from a trap site [41].

TABLE VIII. Desorption activation energies of H as calculated with MTP using Eq. (10).

Site	Activation Energy (eV)
Coherent interstitial	0.22–0.27
Coherent vacancy	1.18
Semicoherent interstitial	0.25–0.31
Semicoherent misfit core	0.20
Semicoherent misfit intersection	0.36
Semicoherent vacancy	1.00–1.04
Incoherent side interface interstitial	0.12–0.20
Incoherent side interface exothermic vacancy	0.53–0.78
Incoherent side interface endothermic vacancy	0.98–1.68
TiC bulk vacancy	1.38

At the interface, because there are several degenerate trap sites in close vicinity, re-trapping events are likely. Drexler *et al*. reinterpreted the data from [17] by taking into account re-trapping events based on the number density and binding energy of the trap sites, and found that the measured activation energies can be significantly lower [47]. Their reported values for the coherent interface range between 0.21 and 0.29 eV. The MTP activation energies for the fully coherent interface range between 0.22 and 0.27 eV, in good agreement with the analysis of Drexler *et al*. [47], as well as DFT reports [30,31].

For semicoherent TiC, desorption activation energies between 0.44 and 0.58 eV are reported [17,22,34]. Although the observed range is not different from the TDS results at the coherent interface, Wei *et al*. attributed these values to misfit dislocations [34]. Later, DFT calculations also showed the misfit-dislocation core to have a desorption activation energy close to 0.5 eV [27]. However, our MTP results yield a value of 0.20–0.36 eV at the semicoherent interface. Because of the highly compressive stresses at the misfit-dislocation core, the cores do not have a higher detrapping activation energy than the coherent regions of the interface, with only a small increase (maximum 0.06 eV) in the regions adjacent to, but not at the core. The activation energy is increased further by 0.05 eV at the intersection point of misfit dislocations. Our calculations support the initial observation that the activation energies are similar for both coherent and semicoherent interfaces. Homogeneous segregation of deuterium atoms at the broad interface of semicoherent TiC has also been observed with APT [120]. While the homogeneity was previously attributed to either uniformly spaced misfit dislocations or vacancies, the MTP calculations suggest that the evenly distributed interstitial sites around the coherency strain fields are probably the sites responsible for segregation.

For incoherent TiC, a wide range of experimental activation energies between 0.55 and 1.50 eV is found, which are attributed to C vacancies inside the carbide [34,40,42]. With the MTP, the incoherent side interface is found to have a wide range of desorption activation energies, ranging between 0.53 and 1.68 eV, depending sensitively upon the local atomic environment of the vacancy as well as the local strain. Also, Wei *et al*. directly estimated the activation energy at the incoherent side interface of semicoherent TiC to be in the range 0.58–1.04 eV [34], which is partly in good agreement with the activation energy from the exothermically formed C vacancies.

H migration

In the aforementioned TDS measurements, it is usually seen that different trap sites are activated depending on the H charging method [45]. Electrochemical H charging, performed at room temperature, is often reported to populate only the low-activation-energy trap sites associated with the interface [34,42]. In order to reach the deep traps (C vacancies), high-temperature gaseous charging is found to be necessary [38,42,44], which brings into question the efficacy of these carbides as irreversible H traps. The barrier for H to migrate from an interstitial site in the Fe matrix at the interface into a C vacancy that lies beyond the first TiC layer (i.e., a scenario in which interface vacancies are not present) is calculated to be 1.45 eV with MTP (the corresponding barrier was reported to be 1.7 eV in an earlier DFT study [27]). For such a highly endothermic process, it is reasonable that high temperatures are a necessity.

Contrarily, some experimental studies have also reported high activation energies after electrochemical charging that could only be ascribed to C vacancies [17,40,121]. Liu *et al.* [121] complemented their experimental observations by also calculating, with DFT, the activation energy for H to migrate into a C vacancy in the bulk of TiC from an interstitial site at the interface via a chain of interconnected vacancies. Such a network has been envisioned to provide an easier pathway for H ingress [27]. For interconnected vacancies from the interface to the second TiC layer, we found the migration barrier to be lowered to 0.62 eV in the coherent regions, and 0.39 eV and 0.31 eV near the misfit-dislocation core and intersection, respectively. If H percolates into C vacancies in the interior of the carbides, our results show that the easiest migration path is through vacancies that lie directly above intersecting misfit dislocations. The MTP also sheds light on the presence of such vacancy networks in TiC. The extremely low formation energy of vacancies along the side interface and above intersecting perpendicular misfit dislocations on the broad face of semicoherent TiC suggests that their presence is highly probable in these regions. The migration barrier for H to get trapped in these interfacial vacancies can be as low as 0.02 eV, making them accessible at lower temperatures. However, our results in Fig. 21 also show that strain-induced vacancy formation is facilitated only in the interface layer, and to some extent in the subsequent layer, but the likelihood of vacancy chains extending far into the bulk of the carbide is low. Combined with the low H diffusivity in bulk TiC, the occupation of all available vacancies in the bulk seems challenging. The difficulty of uniform coverage of bulk TiC with H has been observed by Secondary Ion Mass Spectroscopy, where H was found only at the interface of disk-shaped TiC after gaseous H charging at 700 °C [22]. For maximizing H trapping in C vacancies, smaller (coherent or semicoherent) carbides are therefore more beneficial, as strain-induced vacancies can exist farther into the bulk of the carbide.

V. SUMMARY

To study the intricacies of hydrogen trapping and kinetics in TiC reinforced steels, an Fe-TiC-H machine-learning interatomic potential is developed. A DFT-based training dataset comprising three distinct crystal systems—bcc Fe, rocksalt TiC, and the coherent TiC/Fe interface—with and without hydrogen, is first generated. An MTP is then trained on the dataset, achieving energy and force RMSEs of 3.3 meV/atom and 75 meV/Å, respectively. The MTP shows close agreement with DFT and experimental data for elastic and dynamic properties, vacancy formation energies, hydrogen segregation energies, migration barriers, and hydrogen diffusivity in the bulk phases, as well as structural properties and hydrogen segregation energies at the coherent TiC/Fe interface.

A rigorous treatment of both semicoherent and incoherent side interfaces is performed with MTP. The atomic relaxations near misfit dislocations are found to be significantly different from those obtained with DFT, where small, isolated supercells are used. The dislocation core is found to be highly compressed, resulting in higher hydrogen segregation energies than those obtained with DFT. At the incoherent interface, hydrogen segregation in C vacancies is found to be highly sensitive to the local atomic environment of the vacancy, and a broad range of segregation energies is obtained, unlike at the coherent or semicoherent interface. These results enable a more accurate interpretation of experimental data than previously possible from DFT alone.

The MTP further highlights the efficacy of TiC in trapping hydrogen. As C vacancies are the deepest traps, the percolation of hydrogen to all available C vacancies would maximize the trapping capability of TiC. The MTP results show that strain-induced vacancies can form preferentially near the misfit dislocations, which provide a low-barrier pathway for hydrogen ingress into the bulk of the carbide.

ACKNOWLEDGMENTS

The authors would like to thank Tata Steel Netherlands for sponsoring this research. This project was carried out under Project No. N19009 in the framework of the Partnership Program of the Materials Innovation Institute (M2i) and the Netherlands Organisation for Scientific Research (NWO). This work was facilitated by NWO Domain Science for the use of supercomputer facilities.

DATA AVAILABILITY

The DFT dataset and the Fe–TiC–H MTP are freely available at the 4TU Research Data Repository [122].

APPENDIX A: MTP HYPERPARAMETER OPTIMIZATION

The MTP hyperparameters, force weight (w_f) and cutoff radius (R_c), are optimized through a grid search. The effect of w_f on training errors is shown in Fig. 23(a). Increasing w_f leads to lower force RMSE, which tends to saturate at $w_f \geqslant 0.03$. However, this comes at the cost of increased errors in energy prediction. $w_f = 0.01$ yields the lowest energy RMSE, while the force RMSE is also comparable to its saturated value, making it the optimal choice.

For optimizing R_c, its effect on selected properties of Fe and TiC is evaluated, as shown in Fig. 23(b). These comprise the elastic constants (C11, C12, C44) and bulk modulus (B), Fe (v_{Fe}) and C (v_{TiC}) vacancy formation energy in Fe and TiC,

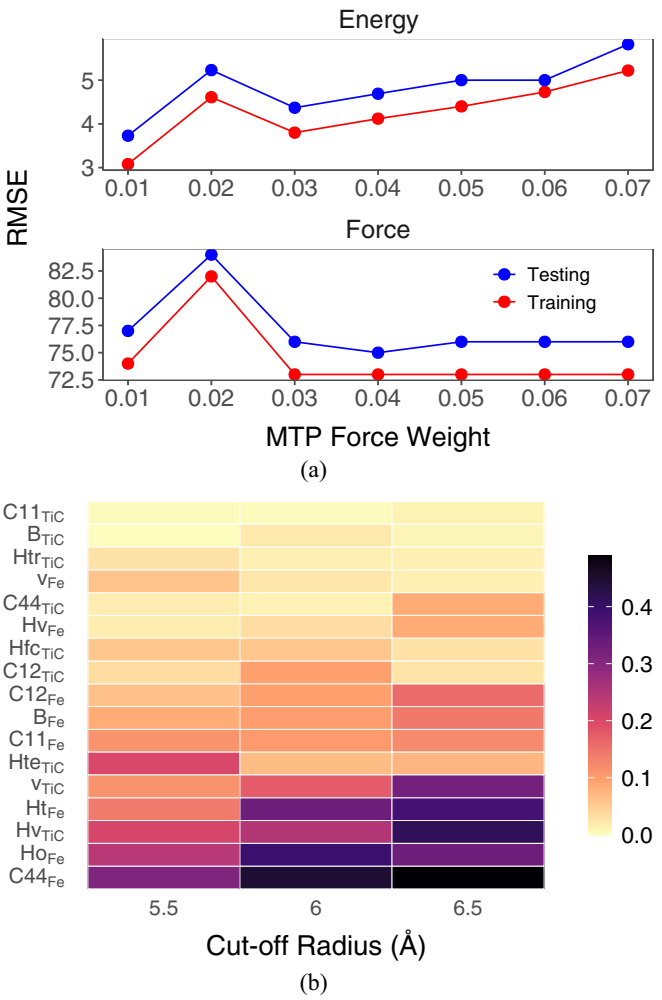


FIG. 23. MTP Hyperparameter optimization. (a) Force weight. Energy and force RMSEs are in meV/atom and eV/Å, respectively. (b) Cutoff radius. Color bar represents relative error in MTP predictions.

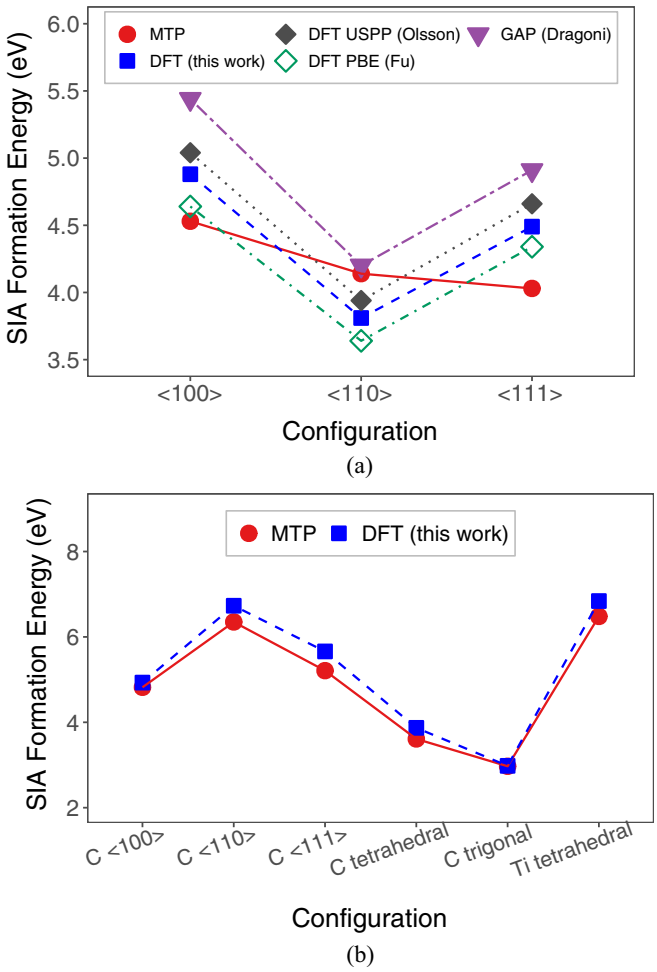


FIG. 24. Formation energy of various self-interstitials in (a) Fe and (b) TiC. DFT Results of Fu *et al*. [98] and Olsson *et al*. [obtained with Ultrasoft Psuedopotential (USPP)] [95], along with the GAP results of Dragoni *et al*. are also shown [66].

the corresponding H segregation energies (Hv_{Fe} and Hv_{TiC}), and H solution enthalpy in the interstitial sites of Fe (Ho_{Fe} and Ht_{Fe} in octahedral and tetrahedral interstices, respectively) and TiC (Htr_{TiC} and Hte_{TiC} in the trigonal and tetrahedral interstices, respectively). R_c values of 5.5 Å, 6 Å, and 6.5 Å are tested. As can be seen in Fig. 23(b), MTP predictions of Ho_{Fe}, Ht_{Fe}, v_{TiC}, Hv_{TiC}, and $C44_{Fe}$ deteriorate with increasing R_c, leading to the selection of 5.5 Å as the optimal value.

The hyperparameter optimization was performed on an earlier iteration of the dataset (7411 configurations); the additional 45 configurations, comprising SIAs in Fe, were added subsequently and do not alter the optimized parameters.

APPENDIX B: INTERSTITIAL FORMATION ENERGIES IN BCC FE AND ROCKSALT TIC

The formation energies of various self-interstitial atom (SIA) configurations in Fe are shown in Fig. 24. The absolute errors in MTP predictions are quite similar (0.3 eV to 0.5 eV) for the three configurations studied here. However, while DFT (and GAP) calculations reveal the ⟨110⟩ configuration to be the most stable [90,95,98], MTP predicts the ⟨111⟩ SIA to be more favorable. Considering the high absolute formation energies of these SIAs, this is not considered a major drawback of the MTP.

SIA formation energies in TiC are shown in Fig. 24(b). MTP predictions of formation energies and preferred configurations are in good agreement with DFT, with a maximum error of 0.05 eV. The same relative stabilities were also found in the DFT calculations of Tsetseris *et al*. [68].

APPENDIX C: INTERSTITIAL FORMATION ENERGY IN THE COHERENT TIC/FE INTERFACE

The formation energies of C and Fe interstitials at the coherent interface are shown in Fig. 25. The preferred C and Fe interstitial configurations are correctly predicted with MTP. In general, there is good agreement between MTP and DFT results.

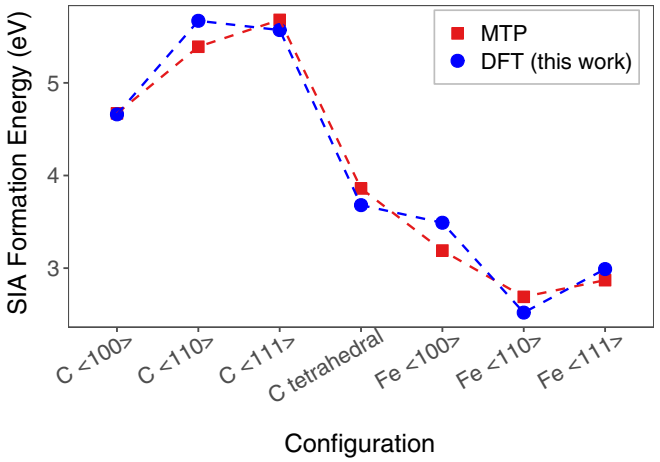


FIG. 25. Formation energy of various self-interstitials at the coherent interface.

APPENDIX D: UNCERTAINTY QUANTIFICATION FOR THE SEMICOHERENT TIC MODEL

In MLIP-2, the uncertainty relating to a configuration is encoded in the extrapolation grade γ [65], which is described briefly here. Following [65], the energy of a configuration as a function of MTP parameters ξ_α of the basis functions B_α is given by

$$E^{mtp}(\xi, cfg) = \sum_{\alpha=1}^{m} \xi_\alpha \sum_i B_\alpha(n_i),$$

where n_i is the atomic neighborhood of atom i. The basis-function evaluations over the entire training set are assembled into a $K \times m$ design matrix

$$\mathbf{B} = \begin{pmatrix} b_1(\mathrm{cfg}_1) & \cdots & b_m(\mathrm{cfg}_1) \\ \vdots & \ddots & \vdots \\ b_1(\mathrm{cfg}_K) & \cdots & b_m(\mathrm{cfg}_K) \end{pmatrix},$$

where K is the total number of configurations, m is the total number of MTP basis functions, and each entry is the evaluation of a basis function on a particular configuration, defined as

$$b_\alpha(\mathrm{cfg_K}) = \sum_i B_\alpha(n_i).$$

From $\mathbf{B}$, an $m \times m$ submatrix $\mathbf{A}$ is then selected using the Maxvol algorithm based on the D-optimality criterion [123], such that $|\det(\mathbf{A})|$ is maximal. The m configurations in $\mathbf{A}$ constitute the active set and represent the most diverse configurations from the point of view of the MTP. It follows that the proximity of a candidate configuration to the training set can be assessed by estimating the change in $|\det(\mathbf{A})|$ if it replaces any of the m configurations in $\mathbf{A}$. The extrapolation grade γ is then defined as

$$(c_1 \cdots c_m) = (b_1 \cdots b_m)\mathbf{A}^{-1},$$
$$\gamma = max\,|c_j|, \quad 1 \leqslant j \leqslant m,$$

where $(b_1 \cdots b_m)$ are the basis function evaluations of the MTP over the candidate configuration and c_j is the corresponding grade when configuration j from the active set is replaced by the candidate configuration. Since $\mathbf{A}$ is originally defined to have a maximal determinant, no configuration in the training set can increase $|\det(\mathbf{A})|$ upon row substitution, which implies $\gamma \leqslant 1$ for all training configurations, while $\gamma > 1$ indicates extrapolation.

The extrapolation grade γ of the semicoherent interface model studied in this work is found to be 0.4, which is well within the interpolation threshold of $\gamma \leqslant 1$. However, this may also reflect the fact that a large fraction of the supercell is coherent-like, which could suppress the configuration-level grade despite locally extrapolative environments near the misfit dislocations. To obtain a per-atom uncertainty estimate around the misfit dislocations, a query-by-committee strategy is employed. Three MTPs are trained on independently (and randomly) drawn 80% subsets of the DFT dataset. The per-atom force uncertainty is defined as

$$\sigma_i^f = \sqrt{\frac{1}{N_c - 1} \sum_{k=1}^{N_c} \left|\mathbf{f}_i^{(k)} - \bar{\mathbf{f}}_i\right|^2},$$

where $\mathbf{f}_i^{(k)}$ is the force on atom i predicted by the kth committee member and $\bar{\mathbf{f}}_i$ is the committee mean. The spatial distribution of σ_i^f around the misfit dislocations is shown

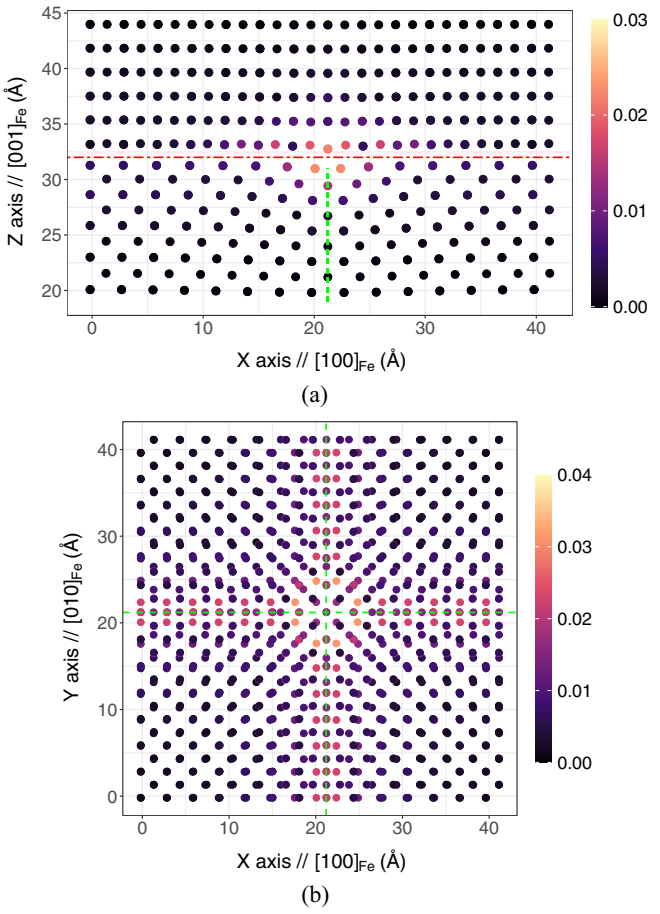


FIG. 26. Per-atom force uncertainty (in eV/Å) around the semicoherent TiC/Fe interface. (a) (010) plane. The interface plane is indicated with a red center line, while the position of the misfit-dislocation core is indicated with a green dashed line (b) (001) plane.

in Fig. 26. Near the dislocation core, the maximum force uncertainty is 25 meV/Å [Fig. 26(a)], rising to 35 meV/Å at the intersection of the perpendicular dislocations [Fig. 26(b)]. Both values are well below the force RMSE of the MTP on the training set (75 meV/Å), confirming that the potential remains accurate in the vicinity of the misfit dislocations.

[1] G. Lovicu, M. Bottazzi, F. D'Aiuto, M. De Sanctis, A. Dimatteo, C. Santus, and R. Valentini, Hydrogen embrittlement of automotive advanced high-strength steels, Metall. Mater. Trans. A **43**, 4075 (2012).

[2] K. Takasawa, R. Ikeda, N. Ishikawa, and R. Ishigaki, Effects of grain size and dislocation density on the susceptibility to high-pressure hydrogen environment embrittlement of high-strength low-alloy steels, Int. J. Hydrogen Energy **37**, 2669 (2012).

[3] Q. Liu, Q. Zhou, J. Venezuela, M. Zhang, and A. Atrens, Hydrogen influence on some advanced high-strength steels, Corros. Sci. **125**, 114 (2017).

[4] S. K. Dwivedi and M. Vishwakarma, Effect of hydrogen in advanced high strength steel materials, Int. J. Hydrogen Energy **44**, 28007 (2019).

[5] Y. Funakawa, T. Shiozaki, K. Tomita, T. Yamamoto, and E. Maeda, Development of high strength hot-rolled sheet steel consisting of ferrite and nanometer-sized carbides, ISIJ International **44**, 1945 (2004).

[6] C. Chen, H. Yen, F. Kao, W. Li, C. Huang, J. Yang, and S. Wang, Precipitation hardening of high-strength low-alloy steels by nanometer-sized carbides, Mater. Sci. Eng. A **499**, 162 (2009).

[7] Y. Funakawa, K. Seto, and H. Nakamichi, Strengthening of ferritic steel by interface precipitated carbides in rows, Mater. Sci. Forum **638–642**, 3218 (2010).

[8] N. Kamikawa, Y. Abe, G. Miyamoto, Y. Funakawa, and T. Furuhara, Tensile behavior of Ti, Mo-added low carbon steels with interphase boundary precipitated structures, Tetsu-to-Hagane **99**, 352 (2013).

[9] N. Kamikawa, M. Hirohashi, Y. Sato, E. Chandiran, G. Miyamoto, and T. Furuhara, Tensile behavior of ferrite-martensite dual phase steels with nano-precipitation of vanadium carbides, ISIJ International **55**, 1781 (2015).

[10] F. Bu, X. Wang, S. Yang, C. Shang, and R. Misra, Contribution of interphase precipitation on yield strength in thermomechanically simulated Ti–Nb and Ti–Nb–Mo microalloyed steels, Mater. Sci. Eng. A **620**, 22 (2015).

[11] S.-P. Tsai, C.-H. Jen, H.-W. Yen, C.-Y. Chen, M.-C. Tsai, C.-Y. Huang, Y.-T. Wang, and J.-R. Yang, Effects of interphase TiC precipitates on tensile properties and dislocation structures in a dual phase steel, Mater. Charact. **123**, 153 (2017).

[12] D. Raabe, B. Sun, A. K. Da Silva, B. Gault, H.-W. Yen, K. Sedighiani, P. T. Sukumar, I. R. Souza Filho, S. Katnagallu, E. Jägle, *et al.*, Current challenges and opportunities in microstructure-related properties of advanced high-strength steels, Metall. Mater. Trans. A **51**, 5517 (2020).

[13] A. Nagao, M. L. Martin, M. Dadfarnia, P. Sofronis, and I. M. Robertson, The effect of nanosized (Ti, Mo)C precipitates on hydrogen embrittlement of tempered lath martensitic steel, Acta Mater. **74**, 244 (2014).

[14] T. Depover, O. Monbaliu, E. Wallaert, and K. Verbeken, Effect of Ti, Mo and Cr based precipitates on the hydrogen trapping and embrittlement of Fe–C–X Q&T alloys, Int. J. Hydrogen Energy **40**, 16977 (2015).

[15] H. K. D. H. Bhadeshia, Prevention of hydrogen embrittlement in steels, ISIJ International **56**, 24 (2016).

[16] T. Depover and K. Verbeken, Hydrogen trapping and hydrogen induced mechanical degradation in lab cast Fe-C-Cr alloys, Mater. Sci. Eng. A **669**, 134 (2016).

[17] T. Depover and K. Verbeken, The effect of TiC on the hydrogen induced ductility loss and trapping behavior of Fe-C-Ti alloys, Corros. Sci. **112**, 308 (2016).

[18] T. Depover and K. Verbeken, Evaluation of the effect of V_4C_3 precipitates on the hydrogen induced mechanical degradation in Fe-C-V alloys, Mater. Sci. Eng. A **675**, 299 (2016).

[19] T. Depover and K. Verbeken, Evaluation of the role of Mo_2C in hydrogen induced ductility loss in Q&T Fe–C–Mo alloys, Int. J. Hydrogen Energy **41**, 14310 (2016).

[20] A. Laureys, L. Claeys, T. De Seranno, T. Depover, E. Van den Eeckhout, R. Petrov, and K. Verbeken, The role of titanium and vanadium based precipitates on hydrogen induced degradation of ferritic materials, Mater. Charact. **144**, 22 (2018).

[21] R. Fernández-Sousa, C. Betegón, and E. Martínez-Pañeda, Analysis of the influence of microstructural traps on hydrogen assisted fatigue, Acta Mater. **199**, 253 (2020).

[22] T. Boot, A. Suresh Kumar, S. Eswara, P. Kömmelt, A. Böttger, and V. Popovich, Hydrogen trapping and embrittlement of titanium- and vanadium carbide-containing steels after high-temperature hydrogen charging, J. Mater. Sci. **59**, 7873 (2024).

[23] R. A. Oriani, A mechanistic theory of hydrogen embrittlement of steels, Ber. Bunsenges. Phys. Chem. **76**, 848 (1972).

[24] J. Song and W. A. Curtin, Atomic mechanism and prediction of hydrogen embrittlement in iron, Nat. Mater. **12**, 145 (2013).

[25] S. Wang, M. L. Martin, P. Sofronis, S. Ohnuki, N. Hashimoto, and I. M. Robertson, Hydrogen-induced intergranular failure of iron, Acta Mater. **69**, 275 (2014).

[26] S. S. Shishvan, G. Csányi, and V. S. Deshpande, Hydrogen induced fast-fracture, J. Mech. Phys. Solids **134**, 103740 (2020).

[27] D. Di Stefano, R. Nazarov, T. Hickel, J. Neugebauer, M. Mrovec, and C. Elsässer, First-principles investigation of hydrogen interaction with TiC in α-Fe, Phys. Rev. B **93**, 184108 (2016).

[28] Y. Ma, Y. Shi, H. Wang, Z. Mi, Z. Liu, L. Gao, Y. Yan, Y. Su, and L. Qiao, A first-principles study on the hydrogen trap characteristics of coherent nano-precipitates in α-Fe, Int. J. Hydrogen Energy **45**, 27941 (2020).

[29] B. Zhang, J. Su, M. Wang, Z. Liu, Z. Yang, M. Militzer, and H. Chen, Atomistic insight into hydrogen trapping at MC/BCC-Fe phase boundaries: The role of local atomic environment, Acta Mater. **208**, 116744 (2021).

[30] S. Sagar, M. H. Sluiter, and P. Dey, First - principles study of hydrogen-carbide interaction in bcc Fe, Int. J. Hydrogen Energy **50**, 211 (2024).

[31] P. Hammer, L. Romaner, and V. I. Razumovskiy, Hydrogen trapping in mixed carbonitrides, Acta Mater. **268**, 119754 (2024).

[32] H. Ding, X. Fan, C. Li, X. Liu, D. Jiang, and C. Wang, First-principles study of hydrogen storage in non-stoichiometric TiC_x, J. Alloys Compd. **551**, 67 (2013).

[33] R. Salehin, G. B. Thompson, and C. R. Weinberger, Hydrogen trapping and storage in the group IVB-VIB transition metal carbides, Materials & Design **214**, 110399 (2022).

[34] F. G. Wei and K. Tsuzaki, Quantitative analysis on hydrogen trapping of TiC particles in steel, Metall. Mater. Trans. A **37**, 331 (2006).

[35] R. G. Baker and J. Nutting, Precipitation processes in steels, Iron and Steel Institute Special Report **64**, 1 (1959).

[36] F.-G. Wei, T. Hara, and K. Tsuzaki, High-resolution transmission electron microscopy study of crystallography and morphology of TiC precipitates in tempered steel, Philos. Mag. **84**, 1735 (2004).

[37] S. Taniguchi, G. Shigesato, and M. Sugiyama, Atomic resolution scanning transmission electron microscopy of TiC precipitates in low carbon ferritic steels, ISIJ International **62**, 984 (2022).

[38] F. G. Wei and K. Tsuzaki, Hydrogen absorption of incoherent TiC particles in iron from environment at high temperatures, Metall. Mater. Trans. A **35**, 3155 (2004).

[39] F.-G. Wei, T. Hara, and K. Tsuzaki, Nano-preciptates design with hydrogen trapping character in high strength steel, in *Advanced Steels: The Recent Scenario in Steel Science and Technology* (Springer, New York, 2011), pp. 87-92.

[40] G. M. Pressouyre and I. M. Bernstein, A quantitative analysis of hydrogen trapping, Metall. Trans. A **9**, 1571 (1978).

[41] F. G. Wei, T. Hara, and K. Tsuzaki, Precise determination of the activation energy for desorption of hydrogen in two Ti-added steels by a single thermal-desorption spectrum, Metall. Mater. Trans. B **35**, 587 (2004).

[42] D. Pérez Escobar, E. Wallaert, L. Duprez, A. Atrens, and K. Verbeken, Thermal desorption spectroscopy study of the interaction of hydrogen with TiC precipitates, Met. Mater. Int. **19**, 741 (2013).

[43] N. Winzer, O. Rott, R. Thiessen, I. Thomas, K. Mraczek, T. Höche, L. Wright, and M. Mrovec, Hydrogen diffusion and trapping in Ti-modified advanced high strength steels, Materials & Design **92**, 450 (2016).

[44] L. Vandewalle, T. Depover, and K. Verbeken, Hydrogen trapping of carbides during high temperature gaseous hydrogenation, Int. J. Hydrogen Energy **48**, 32158 (2023).

[45] L. Vandewalle, T. Depover, and K. Verbeken, Current state-of-the-art of hydrogen trapping by carbides: From theory to experiment, Int. J. Hydrogen Energy **136**, 888 (2025).

[46] T. Boot, P. Kömmelt, H. J. C. Brouwer, A. Böttger, and V. Popovich, Effect of titanium and vanadium nano-carbide size on hydrogen embrittlement of ferritic steels, npj Materials Degradation **9**, 2 (2025).

[47] A. Drexler, T. Depover, K. Verbeken, and W. Ecker, Model-based interpretation of thermal desorption spectra of Fe-C-Ti alloys, J. Alloys Compd. **789**, 647 (2019).

[48] K. Verbeken, Analysing hydrogen in metals: Bulk thermal desorption spectroscopy (TDS) methods, in *Gaseous Hydrogen Embrittlement of Materials in Energy Technologies* (Elsevier, Amsterdam, 2012), pp. 27-55.

[49] F.-G. Wei, M. Enomoto, and K. Tsuzaki, Applicability of the Kissinger's formula and comparison with the McNabb–Foster model in simulation of thermal desorption spectrum, Comput. Mater. Sci. **51**, 322 (2012).

[50] A. Drexler, L. Vandewalle, T. Depover, K. Verbeken, and J. Domitner, Critical verification of the Kissinger theory to evaluate thermal desorption spectra, Int. J. Hydrogen Energy **46**, 39590 (2021).

[51] S. Echeverri Restrepo, D. Di Stefano, M. Mrovec, and A. T. Paxton, Density functional theory calculations of iron-vanadium carbide interfaces and the effect of hydrogen, Int. J. Hydrogen Energy **45**, 2382 (2020).

[52] Y. Li, X. Zhang, T. Wu, J. Tang, L. Deng, W. Li, L. Wang, H. Deng, and W. Hu, First-principles study on the dissolution and diffusion behavior of hydrogen in carbide precipitates, Int. J. Hydrogen Energy **46**, 22030 (2021).

[53] S. Tang, L.-x. Li, Q. Peng, H.-l. Yan, M.-h. Cai, J.-p. Li, Z.-y. Liu, and G.-d. Wang, First-principles insights into hydrogen trapping in interstitial-vacancy complexes in vanadium carbide, Phys. Chem. Chem. Phys. **24**, 20400 (2022).

[54] While the experimental binding energies correspond to desorption, i.e., hydrogen escaping the trap, the segregation energy measured with DFT is defined as the energy related to hydrogen entering the trap, leading to opposite signs of the two energies.

[55] J. Behler and M. Parrinello, Generalized neural-network representation of high-dimensional potential-energy surfaces, Phys. Rev. Lett. **98**, 146401 (2007).

[56] A. P. Bartók, M. C. Payne, R. Kondor, and G. Csányi, Gaussian approximation potentials: The accuracy of quantum mechanics, without the electrons, Phys. Rev. Lett. **104**, 136403 (2010).

[57] J. Behler, Perspective: Machine learning potentials for atomistic simulations, J. Chem. Phys. **145**, 170901 (2016).

[58] Y. Zuo, C. Chen, X. Li, Z. Deng, Y. Chen, J. Behler, G. Csányi, A. V. Shapeev, A. P. Thompson, M. A. Wood, and S. P. Ong, Performance and cost assessment of machine learning interatomic potentials, J. Phys. Chem. A **124**, 731 (2020).

[59] Y. Lysogorskiy, C. v. d. Oord, A. Bochkarev, S. Menon, M. Rinaldi, T. Hammerschmidt, M. Mrovec, A. Thompson, G. Csányi, C. Ortner, and R. Drautz, Performant implementation of the atomic cluster expansion (PACE) and application to copper and silicon, npj Comput. Mater. **7**, 97 (2021).

[60] L. Zhang, G. Csányi, E. van der Giessen, and F. Maresca, Efficiency, accuracy, and transferability of machine learning potentials: Application to dislocations and cracks in iron, Acta Mater. **270**, 119788 (2024).

[61] A. V. Shapeev, Moment tensor potentials: A class of systematically improvable interatomic potentials, Multiscale Model. Simul. **14**, 1153 (2016).

[62] K. Gubaev, V. Zaverkin, P. Srinivasan, A. I. Duff, J. Kästner, and B. Grabowski, Performance of two complementary machine-learned potentials in modelling chemically complex systems, npj Comput. Mater. **9**, 129 (2023).

[63] S. R. Xie, M. Rupp, and R. G. Hennig, Ultra-fast interpretable machine-learning potentials, npj Comput. Mater. **9**, 162 (2023).

[64] K. Gubaev, E. V. Podryabinkin, G. L. Hart, and A. V. Shapeev, Accelerating high-throughput searches for new alloys with active learning of interatomic potentials, Comput. Mater. Sci. **156**, 148 (2019).

[65] I. S. Novikov, K. Gubaev, E. V. Podryabinkin, and A. V. Shapeev, The MLIP package: Moment tensor potentials with MPI and active learning, Mach. Learn.: Sci. Technol. **2**, 025002 (2021).

[66] D. Dragoni, T. D. Daff, G. Csányi, and N. Marzari, Achieving DFT accuracy with a machine-learning interatomic potential: Thermomechanics and defects in BCC ferromagnetic iron, Phys. Rev. Mater. **2**, 013808 (2018).

[67] F.-S. Meng, J.-P. Du, S. Shinzato, H. Mori, P. Yu, K. Matsubara, N. Ishikawa, and S. Ogata, General-purpose neural network interatomic potential for the α-iron and hydrogen binary system: Toward atomic-scale understanding of hydrogen embrittlement, Phys. Rev. Mater. **5**, 113606 (2021).

[68] L. Tsetseris and S. Pantelides, Vacancies, interstitials and their complexes in titanium carbide, Acta Mater. **56**, 2864 (2008).

[69] W. Sun, H. Ehteshami, and P. A. Korzhavyi, Structure and energy of point defects in TiC: An *ab initio* study, Phys. Rev. B **91**, 134111 (2015).

[70] D. H. R. Fors and G. Wahnström, Theoretical study of interface structure and energetics in semicoherent Fe(001)/*MX*(001) systems (*M*=Sc, Ti, V, Cr, Zr, Nb, Hf, Ta; *X*=C or N), Phys. Rev. B **82**, 195410 (2010).

[71] S. Lu, J. Ågren, and L. Vitos, *Ab initio* study of energetics and structures of heterophase interfaces: From coherent to semicoherent interfaces, Acta Mater. **156**, 20 (2018).

[72] Shuichi Nosé, A unified formulation of the constant temperature molecular dynamics methods, J. Chem. Phys. **81**, 511 (1984).

[73] W. G. Hoover, Canonical dynamics: Equilibrium phase-space distributions, Phys. Rev. A **31**, 1695 (1985).

[74] G. Kresse and J. Furthmüller, Efficient iterative schemes for ab initio total-energy calculations using a plane-wave basis set, Phys. Rev. B **54**, 11169 (1996).

[75] J. P. Perdew, K. Burke, and M. Ernzerhof, Generalized gradient approximation made simple, Phys. Rev. Lett. **77**, 3865 (1996).

[76] G. Kresse and D. Joubert, From ultrasoft pseudopotentials to the projector augmented-wave method, Phys. Rev. B **59**, 1758 (1999).

[77] M. Methfessel and A. T. Paxton, High-precision sampling for Brillouin-zone integration in metals, Phys. Rev. B **40**, 3616 (1989).

[78] H. J. Monkhorst and J. D. Pack, Special points for Brillouin-zone integrations, Phys. Rev. B **13**, 5188 (1976).

[79] A. P. Thompson, H. M. Aktulga, R. Berger, D. S. Bolintineanu, W. M. Brown, P. S. Crozier, P. J. in 't Veld, A. Kohlmeyer, S. G. Moore, T. D. Nguyen, *et al.*, LAMMPS - A flexible simulation tool for particle-based materials modeling at the atomic, meso, and continuum scales, Comput. Phys. Commun. **271**, 108171 (2022).

[80] G. Henkelman and H. Jónsson, Improved tangent estimate in the nudged elastic band method for finding minimum energy paths and saddle points, J. Chem. Phys. **113**, 9978 (2000).

[81] G. Henkelman, B. P. Uberuaga, and H. Jónsson, A climbing image nudged elastic band method for finding saddle points and minimum energy paths, J. Chem. Phys. **113**, 9901 (2000).

[82] D. E. Jiang and E. A. Carter, Diffusion of interstitial hydrogen into and through BCC Fe from first principles, Phys. Rev. B **70**, 064102 (2004).

[83] Z. S. Basinski, W. Hume-Rothery, and A. L. Sutton, The lattice expansion of iron, Proc. R. Soc. London A **229**, 459 (1955).

[84] A. Dunand, H. D. Flack, and K. Yvon, Bonding study of TiC and TiN. I. High-precision x-ray-diffraction determination of the valence-electron density distribution, Debye-Waller temperature factors, and atomic static displacements in $TiC_{0.94}$ and $TiN_{0.99}$, Phys. Rev. B **31**, 2299 (1985).

[85] D. L. Price and B. R. Cooper, Total energies and bonding for crystallographic structures in titanium-carbon and tungsten-carbon systems, Phys. Rev. B **39**, 4945 (1989).

[86] G.-X. Zhang, A. M. Reilly, A. Tkatchenko, and M. Scheffler, Performance of various density-functional approximations for cohesive properties of 64 bulk solids, New J. Phys. **20**, 063020 (2018).

[87] J. Neugebauer and T. Hickel, Density functional theory in materials science, WIREs Comput. Mol. Sci. **3**, 438 (2013).

[88] J. Park, B. D. Yu, and S. Hong, van der Waals density functional theory study for bulk solids with BCC, FCC, and diamond structures, Curr. Appl. Phys. **15**, 885 (2015).

[89] J. J. Adams, D. S. Agosta, R. G. Leisure, and H. Ledbetter, Elastic constants of monocrystal iron from 3 to 500 K, J. Appl. Phys. **100**, 113530 (2006).

[90] D. Dragoni, D. Ceresoli, and N. Marzari, Thermoelastic properties of α-iron from first-principles, Phys. Rev. B **91**, 104105 (2015).

[91] M. Khanzadeh and G. Alahyarizadeh, A DFT study on pressure dependency of TiC and ZrC properties: Interconnecting elastic constants, thermodynamic, and mechanical properties, Ceram. Int. **47**, 9990 (2021).

[92] R. Chang and L. J. Graham, Low-temperature elastic properties of ZrC and TiC, J. Appl. Phys. **37**, 3778 (1966).

[93] A. Togo and I. Tanaka, First principles phonon calculations in materials science, Scr. Mater. **108**, 1 (2015).

[94] Y. Tateyama and T. Ohno, Stability and clusterization of hydrogen-vacancy complexes in $\alpha - Fe$: An *ab initio* study, Phys. Rev. B **67**, 174105 (2003).

[95] P. Olsson, C. Domain, and J. Wallenius, *Ab initio* study of Cr interactions with point defects in BCC Fe, Phys. Rev. B **75**, 014110 (2007).

[96] L. De Schepper, D. Segers, L. Dorikens-Vanpraet, M. Dorikens, G. Knuyt, L. M. Stals, and P. Moser, Positron annihilation on pure and carbon-doped α-iron in thermal equilibrium, Phys. Rev. B **27**, 5257 (1983).

[97] Mikael Råsander, H. W. Hugosson, and A. Delin, Density functional study of carbon vacancies in titanium carbide, J. Phys.: Condens. Matter **30**, 015702 (2018).

[98] C.-C. Fu, F. Willaime, and P. Ordejón, Stability and mobility of Mono- and Di-interstitials in α-Fe, Phys. Rev. Lett. **92**, 175503 (2004).

[99] D. C. Sorescu, First principles calculations of the adsorption and diffusion of hydrogen on Fe(100) surface and in the bulk, Catal. Today **105**, 44 (2005).

[100] A. S. Kholtobina, R. Pippan, L. Romaner, D. Scheiber, W. Ecker, and V. I. Razumovskiy, Hydrogen trapping in BCC iron, Materials **13**, 2288 (2020).

[101] E. Hayward and C.-C. Fu, Interplay between hydrogen and vacancies in α-Fe, Phys. Rev. B **87**, 174103 (2013).

[102] F. Besenbacher, S. M. Myers, P. Nordlander, and J. K. Norskov, Multiple hydrogen occupancy of vacancies in Fe, J. Appl. Phys. **61**, 1788 (1987).

[103] C. Stampfl, W. Mannstadt, R. Asahi, and A. J. Freeman, Electronic structure and physical properties of early transition metal mononitrides: Density-functional theory LDA, GGA, and screened-exchange LDA FLAPW calculations, Phys. Rev. B **63**, 155106 (2001).

[104] J. C. Stotts, R. Salehin, I. N. Bakst, G. B. Thompson, and C. R. Weinberger, Hydrogen diffusion and storage in substoichiometric TiC, Int. J. Hydrogen Energy **50**, 512 (2024).

[105] M. Råsander, B. Sanyal, U. Jansson, and O. Eriksson, A first principles study of the stability and mobility of defects in titanium carbide, arXiv:1303.2848v1.

[106] M. A. A. Hasan, J. Wang, Y. C. Lim, A. Hu, and S. Shin, Concentration dependence of hydrogen diffusion in α-iron from atomistic perspectives, Int. J. Hydrogen Energy **44**, 27876 (2019).

[107] R. Oriani, The diffusion and trapping of hydrogen in steel, Acta Metall. **18**, 147 (1970).

[108] M. Nagano, Y. Hayashi, N. Ohtani, M. Isshiki, and K. Igaki, Hydrogen diffusivity in high purity alpha iron, Scr. Metall. **16**, 973 (1982).

[109] H. Hagi, Diffusion coefficient of hydrogen in iron without trapping by dislocations and impurities, Mater. Trans. JIM **35**, 112 (1994).

[110] H. Kwon, M. Shiga, H. Kimizuka, and T. Oda, Accurate description of hydrogen diffusivity in BCC metals using machine-learning moment tensor potentials and path-integral methods, Acta Mater. **247**, 118739 (2023).

[111] W.-S. Jung, S.-C. Lee, and S.-H. Chung, Energetics for interfaces between Group IV transition metal carbides and BCC iron, ISIJ International **48**, 1280 (2008).

[112] J. D. Eshelby, Distortion of a crystal by point imperfections, J. Appl. Phys. **25**, 255 (1954).

[113] J. Eshelby, The continuum theory of lattice defects, in *Solid State Physics* (Elsevier, Amsterdam, 1965), pp. 79–144.

[114] M. Akhlaghi, T. Steiner, S. Meka, A. Leineweber, and E. Mittemeijer, Lattice-parameter change induced by accommodation of precipitate/matrix misfit; misfitting nitrides in ferrite, Acta Mater. **98**, 254 (2015).

[115] C. Ioannidou, Z. Arechabaleta, A. Navarro-López, A. Rijkenberg, R. M. Dalgliesh, S. Kölling, V. Bliznuk, C. Pappas, J. Sietsma, A. A. van Well, and S. E. Offerman, Interaction of precipitation with austenite-to-ferrite phase transformation in vanadium micro-alloyed steels, Acta Mater. **181**, 10 (2019).

[116] N.-Y. Park, J.-H. Choi, P.-R. Cha, W.-S. Jung, S.-H. Chung, and S.-C. Lee, First-principles study of the interfaces between Fe and transition metal carbides, J. Phys. Chem. C **117**, 187 (2013).

[117] Y. Kobayashi, J. Takahashi, and K. Kawakami, Experimental evaluation of the particle size dependence of the dislocation–particle interaction force in TiC-precipitation-strengthened steel, Scr. Mater. **67**, 854 (2012).

[118] H. Sawada, S. Taniguchi, K. Kawakami, and T. Ozaki, Transition of the interface between iron and carbide precipitate from coherent to semi-coherent, Metals **7**, 277 (2017).

[119] M. Yao, P. Dey, J.-B. Seol, P. Choi, M. Herbig, R. Marceau, T. Hickel, J. Neugebauer, and D. Raabe, Combined atom probe tomography and density functional theory investigation of the Al off-stoichiometry of κ-carbides in an austenitic Fe–Mn–Al–C low density steel, Acta Mater. **106**, 229 (2016).

[120] J. Takahashi, K. Kawakami, Y. Kobayashi, and T. Tarui, The first direct observation of hydrogen trapping sites in TiC precipitation-hardening steel through atom probe tomography, Scr. Mater. **63**, 261 (2010).

[121] P.-Y. Liu, B. Zhang, R. Niu, S.-L. Lu, C. Huang, M. Wang, F. Tian, Y. Mao, T. Li, P. A. Burr, *et al.*, Engineering metal-carbide hydrogen traps in steels, Nat. Commun. **15**, 724 (2024).

[122] S. Sagar, P. Dey, and F. Maresca, DFT dataset for Fe-TiC-H machine learning interatomic potentials, 2026, doi:10.4121/85896637-392D-4E6F-BDC1-86C1B4A1B863.

[123] V. Olshevsky and E. E. Tyrtyshnikov (ed.), Matrix methods: theory, algorithms, and applications (World Scientific, Singapore, 2010).